



Tailoring the metal-perovskite interface for promotional steering of the catalytic NO reduction by CO in the presence of H₂O on Pd-lanthanum iron manganite composites

Asghar Mohammadi ^a, Ali Farzi ^a, Christoph Thurner ^b, Bernhard Klötzer ^b, Sabine Schwarz ^c, Johannes Bernardi ^c, Aligholi Niaezi ^a, Simon Penner ^{b,*}

^a Reactor & Catalyst Research Lab, Department of Chemical and Petroleum Engineering, University of Tabriz, Tabriz, Iran

^b Institute of Physical Chemistry, University of Innsbruck, Innrain 52c, A-6020 Innsbruck, Austria

^c University Service Centre for Transmission Electron Microscopy, Technische Universität Wien, A-1040 Wien, Austria



ARTICLE INFO

Keywords:

Perovskite
Palladium
Phase boundary
DeNO_x catalysis
Reaction kinetics

ABSTRACT

We steer the catalytic performance and morphology of Pd – lanthanum iron manganite (LFM) perovskite interfaces towards optimum NO+CO reactivity in presence of water by following different preparation approaches. Strong CO adsorption for samples without Pd-perovskite interface acts as an inhibitor for adsorption/dissociation of NO, while samples with an extended interface, additionally aided by H₂O, show reduced CO poisoning. The optimized use of lattice oxygen for CO oxidation at the phase boundary and its replenishment from NO dissociation allows for the formation of more poisoning-resistant active sites for NO activation. Reaction of species from H₂O dissociation with adsorbed CO assists further surface clean off. Enhanced NO reduction activity on the “de-poisoned” interface leads to a pronounced increase in N₂ selectivity. Preferred production of NH₃ at low NO and high CO and H₂O concentration indicates that water gas shift intermediates are linked to increased surface hydrogen activity and increased NH₃ formation.

1. Introduction

NO_x and CO are two major pollutants emitted during combustion of hydrocarbon-based fuels by motor vehicles with significant negative impact on human health and environment. For conventional gasoline engines, three-way catalysts (TWC) can reduce toxic gases effectively under stoichiometric conditions [1–3]. While ceria-zirconia-supported noble metal catalysts meet the current need for highly durable, sintering- and poisoning-resistant catalyst systems, there is strong demand for approaches that enable less use of costly noble metals while maintaining, or even improving, low temperature performance.

Perovskites with the usual ABO₃ stoichiometry were developed as efficient materials for low-cost automotive catalysts due to their exhibit excellent redox properties, high thermal durability and reversible oxygen uptake and release capability [4–6]. The structural and physico-chemical properties of the perovskite catalysts are related to their A and/or B site cations and can be tuned by partial substitution with other metals, yielding a wide variety of sub-stoichiometric structures [7]. La-based (layered) perovskites frequently used for NO reduction by CO

include La(Fe, Mn)O₃ [8], La_{1-x}Sr_xFeO₃ [9], La_{1-x}Sr_xCe_yFeO₃ [10], La₂CuO₄ [11], La(Cr, Mn, Co, Ni)O₃ [12], LaCoO₃ [12], LaCo_{1-x}Cu_xO₃ [13] and LaMn_xCo_{1-x}O₃ [14]. Lanthanum ferrite LaFeO₃ was the most active catalyst among different transition-metal LaBO_{3-δ} perovskites (B = Mn, Fe, Co, Ni and Cu). LaFe_{0.7}Mn_{0.3}O₃ (LFM) showed particularly promising catalytic properties among Mn, Co and Cu-doped lanthanum ferrite catalysts [15,16]. Perovskite deNO_x activity can already be enhanced by very small noble metal amounts [17].

Pd exhibits a good resistance to thermal sintering and features excellent activity for hydrocarbon and carbon monoxide oxidation [18–20]. Generally, the redox chemistry of perovskites under alternating reductive and oxidative treatments determines their bulk or surface structural changes directly, affecting the chemical environment and the oxidation state of the noble metal dopants. Enhancement of NO dissociation is agreed upon as key step in the deNO_x process on Pd - reducible oxide interfaces and also on reduced metal (Pd⁰) sites [21–23]. Water vapor as a major component of the exhaust flow can have a significant effect on catalyst performance and product selectivity. However, despite numerous studies on different aspects of the “dry” NO+CO

* Corresponding author.

E-mail address: simon.penner@uibk.ac.at (S. Penner).

reaction on different catalysts, [18,24–30] studies on the effect of added water vapor are limited [24,31–35]. As many of the elementary steps of the reaction can be same under both dry and wet conditions, a comparative study of the NO+CO reaction under dry and wet conditions allows to clarify water-related mechanistic aspects of the reaction and steering of water-mediated product pathways.

To study the Pd-perovskite interaction and the associated phase boundary effects in detail, we take advantage of a synthesis protocol allowing us to directly compare the catalytic properties of Pd particles on the surface of a $\text{LaFe}_{0.7}\text{Mn}_{0.3}\text{O}_3$ perovskite with a Pd-doped $\text{LaFe}_{0.7}\text{Mn}_{0.3}\text{O}_3$ (i.e., Pd fully incorporated into the perovskite structure) and with both Pd-free (pure LFM) and LFM-free (Pd particles on Al_2O_3) benchmark states. By deliberately exceeding the Pd doping capacity of the perovskite, we can also assess the structural and electronic properties of those exsolved Pd particles in contact with the perovskite. Relating the catalytic properties to the surface chemistry and especially the redox properties (which are directly involved in elementary reaction steps), we can directly infer the intrinsic properties of the differently synthesized Pd-perovskite interfaces, yielding structure-property relationships. This combined effort not only leads to a promising model catalyst with superior activity for automotive emissions control, but also allows drawing definite mechanistic conclusions. Specifically, undoped $\text{LaFe}_{0.7}\text{Mn}_{0.3}\text{O}_3$ and two Pd-doped samples, $\text{La}(\text{Fe}_{0.7}\text{Mn}_{0.3})_{0.98}\text{Pd}_{0.02}\text{O}_{3-\delta}$ (termed “LaPd0.02SG” in the following) and $\text{La}(\text{Fe}_{0.7}\text{Mn}_{0.3})_{0.90}\text{Pd}_{0.10}\text{O}_{3-\delta}$ (termed “LaPd0.1SG” in the following) exhibiting two different nominal Pd loadings, were prepared by a well-established sol-gel method [36]. In LaPd0.02SG, all Pd is incorporated in the perovskite structure, but for LaPd0.1SG, Pd is partially incorporated, but a considerable amount is found on the perovskite surface already in the calcined state. Both doped samples, hence, differ from the two Pd impregnated perovskite catalysts, $\text{Pd/LaFe}_{0.7}\text{Mn}_{0.3}\text{O}_3$, with the same nominal Pd loadings (termed “LaPd0.02IM” and “LaPd0.1IM”) with respect to both bulk and surface Pd distribution. Qualitative and quantitative X-ray powder diffraction (XRD) and transmission electron microscopy (TEM) were used for structural analysis. The quantitative redox chemistry was assessed by detailed temperature-programmed volumetric reduction and oxidation treatments. Surface chemical analysis was based on X-ray photoelectron spectroscopy (XPS). Catalytic testing was performed in a flow reactor for the reduction of NO with CO in the presence and absence of H_2O to investigate the characteristic activity and selectivity patterns of the catalysts, complemented by isothermal steady state experiments to extract key catalytic parameters such as the reaction orders with respect to the NO, CO and H_2O concentration. The latter approach is used to quantitatively test the potential poisoning of the respective active sites during the NO reduction by CO under dry and wet conditions. Our results show, by comparison to the benchmark states, that the main role of the Pd-perovskite phase boundary is to ease the oxidation of carbonaceous species to CO_2 and to reduce CO poisoning effects. This in turn leads to enhanced dissociative absorption and conversion of NO. This promotional mechanism also works better in the presence of H_2O , which is due to the improved surface cleaning process due to the additional clean-off reaction of C1 species with activated/dissociated water.

2. Experimental

2.1. Catalyst preparation

A sol-gel synthesis approach using the metal nitrate precursor materials ($\text{La}(\text{NO}_3)_3 \cdot 6\text{H}_2\text{O}$, $\text{Pd}(\text{NO}_3)_2 \cdot 2\text{H}_2\text{O}$, $\text{Mn}(\text{NO}_3)_2 \cdot 4\text{H}_2\text{O}$, $\text{Fe}(\text{NO}_3)_3 \cdot 9\text{H}_2\text{O}$), was followed for preparation of the pure lanthanum iron manganite (LFM) and the Pd-doped samples with different nominal Pd contents (LaPd0.02SG and LaPd0.1SG) [36]. Final calcination for 5 h at 700 °C yielded the oxidized starting materials. A conventional wet impregnation approach was used for preparation of the Pd-supported perovskite catalysts with the same nominal Pd loadings (LaPd0.02IM and LaPd0.1IM). After dissolving the required amounts of Pd

$(\text{NO}_3)_2 \cdot 2\text{H}_2\text{O}$ and adding the required amount of the calcined LFM perovskite powder in 50 mL of deionized water, the solution was stirred at 25 °C for 1 h, followed by water evaporation at 65 °C. The catalysts were subsequently dried at 80 °C for 12 h and finally calcined at 600 °C for 5 h in air. The LFM-free impregnated 2 wt% Pd/ Al_2O_3 benchmark catalyst was synthesized by the similar wet impregnation approach discussed above.

2.2. Bulk structural characterization

BET-based specific surface areas were measured using a Quantachrome Nova 2000e surface and pore size analyzer and liquid N_2 as adsorbent. Before testing, the samples were degassed at 270 °C in vacuo for 1 h.

The *ex situ* X-ray diffraction data were collected using a STOE STADI P X-ray powder diffractometer in transmission geometry and $\text{Mo K}\alpha$ ($\lambda = 0.7093 \text{ \AA}$) radiation using a focusing $\text{Ge}(111)$ primary beam monochromator, as well as a MYTHEN K linear position-sensitive detector system. Structure analysis is based on the references from the Crystallography Open Database (COD) using the *Fullprof* software tool.

Transmission electron microscopy (TEM) measurements were carried out using a FEI Tecnai F20 S-TWIN analytical (high-resolution) transmission electron microscope (200 kV), equipped with an Apollo XLTW SDD X-ray detector (for collecting energy-dispersive X-ray (EDX) data). For analysis, the powders were supported on holey carbon films grown on Cu grids without further treatment. A standard single-tilt beryllium holder was used for the EDX measurements.

2.3. Surface chemical characterization

X-ray photoelectron spectroscopy (XPS) measurements were performed to evaluate the near-surface chemistry of the constituting elements using a VG ESCALAB apparatus and a monochromated $\text{Al-K}\alpha$ X-ray source ($E = 1487 \text{ eV}$). XP spectra were collected after initial calcination of the samples. For analysis, the sample powders were placed on standard stainless-steel holders without further treatment and fixed by conducting silver paste. Chemical shifts were calibrated by setting the C-C component of the C 1s peak (adventitious carbon) at 284.8 eV. Oxidation states were determined by fitting and de-convoluting the XP spectra using the CasaXPS software tool. The XPS fitting procedure and software settings are discussed in detail in Ref. [18] and in the Supporting Information.

2.4. Volumetric adsorption techniques

An all-quartz tubular reactor (volume 34.50 mL) was used for temperature-programmed reaction and desorption measurements (flowing- O_2 treatment, H_2/CO -TPR, TPD, NO/O_2 -TPO). A quadrupole mass spectrometer setup (QMS, Balzers) allowed us to detect and quantify uptake, desorption and consumption of the reactant gases at each temperature. For quantitative analysis, the relevant gases were detected and calibrated via their respective molecular ions: CO/N_2 ($m/z = 28$), NO ($m/z = 30$), O_2 ($m/z = 32$), Ar ($m/z = 40$) and $\text{N}_2\text{O}/\text{CO}_2$ ($m/z = 44$). The CO signal was corrected for CO_2 fragmentation. Depending on the specific experiment and presence of different gases in the system, simultaneous recording of the mass signals, including the $m/z = 22$ intensities, allowed to disentangle the superimposed intensity contributions of CO_2 and N_2O .

In each experimental sequence, a defined amount of about 60 mg of the powder sample was fixed by quartz wool in the reactor in a chemically inert environment. During the temperature-programmed hydrogen reduction (H_2 -TPR), moisture produced from the sample was removed using a degassed zeolite as water trap installed outside of the heated reaction zone (i.e., sample and zeolite can be heated separately). A Linn High-Term tube furnace was used for heating the sample. The temperature is measured by a Ni/NiCr thermocouple placed near the sample.

The pressure in the reactor system was measured using a differential Baratron® pressure transducer (MKS Instruments). A cold cathode ionization gauge (Balzers, 10^{-8} – 10^{-4} mbar) was used to measure the pressure in the high-vacuum pumping and analysis system. High-vacuum conditions (base pressure 2×10^{-7} mbar) were ensured by a Pfeiffer HiCube turbo molecular pumping station. The reactor pressure and the sample temperature are recorded using a home-designed National Instruments LabVIEW® program.

All gases used in the temperature-programmed experiments (CO/He/O₂/H₂/NO/Ar, Messer Gases) are used in purities of 4.7/5 /3.5 /5.0 /2.5 /5.0, respectively. Before each experimental sequence, the sample was oxidatively pre-treated in flowing oxygen (0.8 mL s⁻¹ ca. 1170 mbar O₂) to remove possible organic compounds and to define a standardized initial oxygen vacancy concentration for all samples. Residual moisture was removed from O₂ by an ethanol/liquid N₂ cooling trap (-110 °C). The samples were heated from room temperature to 700 °C within 30 min followed by an isothermal period at 700 °C for 45 min. The samples could cool down to room temperature within 50 min. Finally, the zeolite was degassed under active pumping and heated at 300 °C until the reactor pressure decreased below 10⁻⁶ mbar. After the O₂ pre-treatment and degassing of the zeolite, two different sequences of experiments as defined below were performed on the samples to evaluate their redox chemistry and capacity to form and quench oxygen vacancies. Details on the operation and quantitative analysis are stated in the [Supporting Information](#).

H₂/CO reduction sequence (static = without gas flow to QMS; quasi-static: slow pressure drop due to gas flow to QMS corrected via simultaneous Ar signal drop):

1. Static H₂/quasi-static CO temperature-programmed reduction (H₂-TPR, CO-TPR),
2. Quasi-static NO temperature-programmed oxidation (NO-TPO).

2.5. Catalytic testing in the reduction of NO by CO in the presence and absence of H₂O

200 mg of catalyst powder was fixed with quartz wool in a home-built 8 mm (inner diameter) quartz tube flow reactor setup under atmospheric pressure and total flow rate of 200 mL min⁻¹ (CO: NO: He = 1:1:98 mL min⁻¹ in dry and CO: NO: H₂O:He = 1:1:5:93 mL min⁻¹ under wet conditions, GHSV = 9000 h⁻¹). In each catalytic test, the reactor was heated with a tubular furnace (Linn High Therm) at 2 °C min⁻¹ to 650 °C followed by an isothermal period at 650 °C for 30 min. An external S-type thermocouple (calibrated by an independent experiment with flowing helium) was placed in close contact to the reactor tube to ensure correct temperature reading. H₂O in the reactor inlet was supplied by passing He stream through the water bubbler and its partial pressure was adjusted by both He flow rate and water bubbler temperature based on the saturation vapor pressure of water. The gas line was heated to prevent condensation. The output gas was directly detected by a gas phase infrared spectroscopy (Agilent Cary 660 FT-IR) setups and a quadrupole mass spectrometer (Balzers QME 125). N₂ formation rates were determined by difference from the measured rates of NO consumption and of N₂O and NH₃ formation (by infrared spectroscopy), and confirmed by mass spectrometry (Balzers QME 125). In the steady state experiments, NO consumption and N₂O, NH₃, and N₂ formation rates are reported as moles of consumption or formation normalized to the Pd g [mol(g Pd)⁻¹]. The number of reacted / produced component molecules per second passing through the catalyst bed can be calculated by applying the ideal gas law (using atmospheric pressure and the average gas temperature) [18].

To display the catalytic activity as a function of temperature, we use the following equation to calculate the NO conversion:

$$NO_{\text{Conversion}} = 100 * (1 - \frac{[NO]_{\text{out}}}{[NO]_{\text{in}}})$$

[NO]_{out} and [NO]_{in} indicate the inlet and outlet concentration of NO, respectively.

The impact of mass transport limitations in the chosen reactor setup has been thoroughly assessed and found to be negligible. For details of calculation we refer to the SI. Heat transfer limitations also play a small role due to the low reaction rate and consequently, small local temperature gradients. In addition, the use of helium with high thermal conductivity assures a uniform reactor bed temperature [37]. In order to reflect strict kinetic effects and provide differential reactor conditions, a very small amounts of catalyst (different for each catalyst) was diluted with ground quartz wool for kinetic studies.

3. Results and discussion

3.1. Characterization of the bulk structural changes induced by pre-reduction and NO+CO+H₂O reaction

The specific surface area of the catalysts after initial calcination was determined by BET ([Table 1](#)). All catalysts exhibit an area of 7–14 m² g⁻¹. While the surface areas of the impregnated catalysts are less affected and show comparable surface areas to undoped LFM, incorporation of Pd into the perovskite lattice leads to a slight decrease in the surface area, which might be related to partial blocking of perovskite pores and/or changing its crystallite size by Pd doping.

The summarized X-ray diffraction results after initial calcination, after reduction of NO by CO under dry and wet conditions and after different redox treatments are discussed in the context of [Figs. S1–S4](#) (cf. [SI, Section B](#)). All catalysts are mainly crystallized in the parent cubic LaFeO₃ perovskite structure, except LaPd0.1SG, which cannot accommodate all the Pd in its structure and the excess Pd crystallizing as PdO in a separate phase on the perovskite surface. The removal of Pd from the lattice proceeds without distorting the perovskite structure. The very broad PdO peak in LaPd0.1IM XRD patterns indicates the presence of rather small or disordered PdO particles. Reduction leads to a reversible cubic-orthorhombic structural transition of pure LFM. At low Pd loadings, the perovskite bulk changes are similar to pure LFM. Irreversible Pd-related changes appear at higher Pd loadings and result from the sintering of Pd particles during reduction. Both Pd- and perovskite-related structural changes during the NO reduction by CO under both wet and dry condition are moderate. These observations are reasonable, as the NO+CO (+ H₂O) reactions are redox reactions [38], and reduction and re-oxidation processes occur simultaneously. These results indicate partial reduction of the catalysts during the NO reduction by CO under both dry and wet conditions.

To visualize the distribution of Pd on and within the perovskite, a thorough TEM analysis was performed on all catalysts after initial calcination and, moreover, on LaPd0.02SG and LaPd0.1IM also after CO reduction. The TEM analysis of LaPd0.02SG ([Fig. 1](#)) reveals a dense assembly of nm-to μ m-sized polycrystalline perovskite grains (Panels A and B). The presence of the cubic perovskite structure is verified by HRTEM (Panel C). Lattice fringes of 0.4 nm are related to the (100) crystal planes ($d_{\text{theor}}(100) = 0.393$ nm [39]). In Panel D, the HAADF image and the EDX maps reveal a uniform chemical distribution of all elements. The intensity of Pd matches those of both Mn-K and La-L, indicating Pd incorporation into the perovskite structure partially at both the A- and the B-site. The successful introduction of Pd into the perovskite lattice is also confirmed by the absence of small Pd particles in the nm-sized regime or any larger agglomerates of Pd. This then excludes the presence of e.g., X-ray amorphous or nano-sized small crystalline Pd particles not detected by XRD. XPS (cf. [SI, Section D](#)) and TPR (cf. [Section 3.3](#)) results support this claim. CO reduction at 700 °C has no effect on the elemental distribution, and specifically, no exsolution phenomena are observed (cf. [SI, Section C](#), [Fig. S5](#)).

The TEM analysis of LaPd0.10SG and LaPd0.02IM catalysts are highlighted in [Figs. S6–S8](#) in [SI, Section C](#). The presence of both the

Table 1

Overview of catalyst composition, Pd loading, Rietveld-derived cell parameters of the undoped, Pd-doped and Pd-impregnated perovskite structures and associated surface areas.

Catalyst compositions	Acronym	Pd/wt%	Cell parameter/Å	BET/m ² g ⁻¹
LaFe _{0.7} Mn _{0.3} O ₃	LFM	–	3.9097	13
La(Fe _{0.7} Mn _{0.3}) _{0.98} Pd _{0.02} O ₃	LaPd0.02SG	0.5	3.9144	7
La(Fe _{0.7} Mn _{0.3}) _{0.90} Pd _{0.10} O ₃	LaPd0.1SG	2.6	Perovskite: 3.9157 PdO: a = b = 3.0405, c = 5.3235	11
0.87 wt% Pd/LaFe _{0.7} Mn _{0.3} O ₃	LaPd0.02IM	0.6	3.9079	13
4.30 wt% Pd/LaFe _{0.7} Mn _{0.3} O ₃	LaPd0.1IM	2.7	3.9078	14

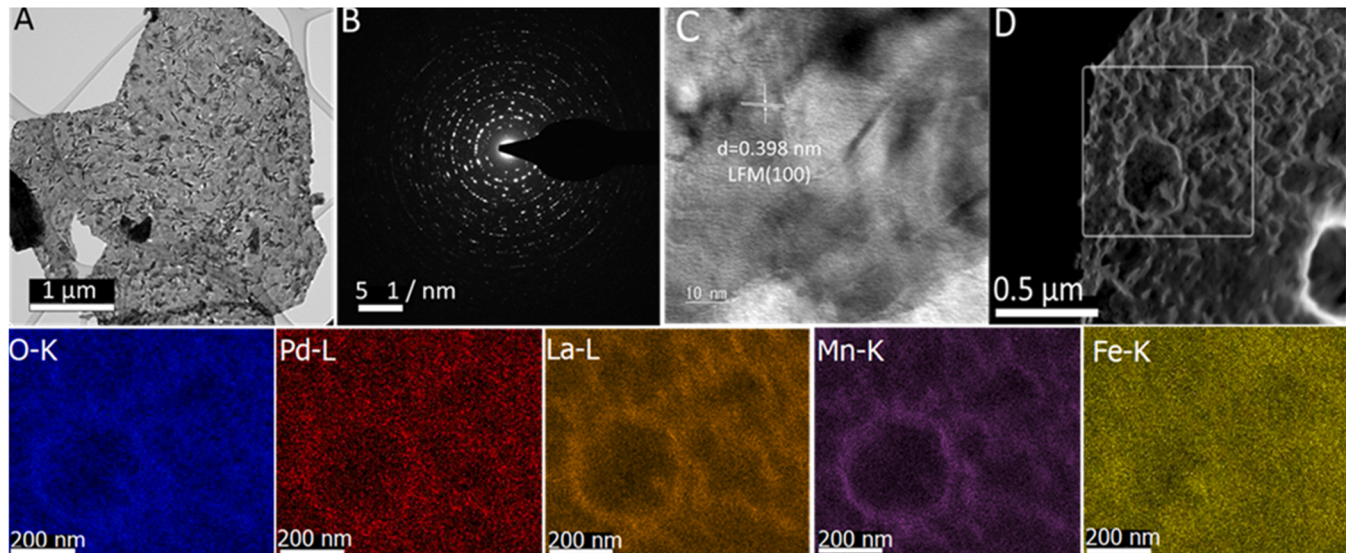


Fig. 1. TEM analysis of LaPd0.02SG after calcination at 700 °C. Panel A: Bright field overview image. Panel B: Selected area electron diffraction (SAED) pattern. Panel C: HRTEM image of a representative perovskite region. Panel D: HAADF image of a perovskite grain edge. Bottom row: EDX maps of relevant elements of the highlighted region in the HAADF image (O-K blue, Pd-L red, La-L yellow, Mn-K purple, Fe-K olive).

perovskite and PdO structures and nonuniform distribution of Pd in LaPd0.10SG confirm the XRD results. In comparison to the impregnated samples, these large PdO particles are less dispersed and feature a less extended interface with the perovskite. HRTEM confirms the presence of metallic Pd in LaPd0.02IM already in the calcined state. The Pd distribution is not uniform and also Pd particles are observed (one is marked by a red arrow in Fig. S7, Panels A and B).

Fig. 2 highlights the TEM analysis of LaPd0.1IM. SAED patterns from a Pd-rich area shows both Pd (111) and LFM (110) reflections. Like for LaPd0.02IM, EDX maps reveal a non-uniform Pd distribution and/or surface enrichment of Pd. The metallic Pd grains on the perovskite surface appear mostly single crystalline. The presence of metallic Pd for the impregnated catalyst indicates that either the 600 °C calcination in static air was not enough to obtain fully oxidized PdO particles [40] or PdO was already partially decomposed at 600 °C (in fact, the thermal decomposition of PdO is reported to be very support-dependent [41]). The enrichment of PdO at the surface is confirmed by XPS (cf. SI, Section D, Fig. S13) for the impregnated catalysts, but is difficult to detect by TEM images, which is also due to the low contrast of Pd on the perovskite. We conclude that the calcination temperature (600 °C) causes agglomeration of metallic Pd particles.

Figs. S9 and S10 (cf. Section C in the SI) show that the initially high Pd(O) dispersion of the Pd-impregnated calcined catalysts decreases after CO reduction, in contrast to LaPd0.1SG, where the dispersion was already initially low, because of exceeding the Pd solubility limit of the perovskite. Apparently, at least the initial Pd(O) dispersion on the surface of the impregnated perovskites is higher. Summarizing the structural properties of the Pd-perovskite materials as derived from combined TEM and XRD analysis we note that for LaPd0.02SG all Pd is and remains

incorporated and for LaPd0.1SG a pronounced rather sharp PdO peak, indicating the preparation-induced presence of crystalline large PdO particles, is visible from the beginning. For LaPd0.02IM, the amount of Pd(O) is too low to be reliably detected by either TEM or XRD, as we assume very small Pd(O) particles. For LaPd0.1IM, a very broad PdO feature is visible in the XRD patterns of the calcined state, indicating very small quasi-amorphous and TEM-invisible PdO particles. Important for the interpretation of the NO reduction by CO reaction profiles, a relatively low initial abundance of Pd(O)-LFM interfacial sites at the surface can be assumed for the sol-gel catalysts and reaction-induced enrichment of these sites by CO under deNO_x conditions appears to be suppressed.

3.2. Catalytic testing in the NO reduction by CO in the presence of H₂O

The temperature dependence of NO conversion and product distribution in the NO reduction by CO in presence of 5% water ("wet conditions") (Fig. 3) reveals that the conversion is very sensitive to the catalyst structure and significantly affects the product distribution. In order to study the effects of water in the NO + CO reaction, we performed the corresponding catalytic experiments also in the absence of water ("dry conditions", Fig. S14). For clarifying Pd - perovskite phase boundary effects, the conversion in the presence of water is compared to a 2 wt% Pd/Al₂O₃ catalyst in Fig. S15, which directly demonstrates the influence of the Pd-perovskite interface by higher NO conversion at lower temperatures for the Pd-impregnated samples. The NO conversion over pure LFM starts at 220 °C (Panel A), reaching 80% at 600 °C. Unlike under wet conditions, under dry conditions (Fig. S14, Panel A), the NO conversion on this catalyst starts at 200 °C and reaches 100% at

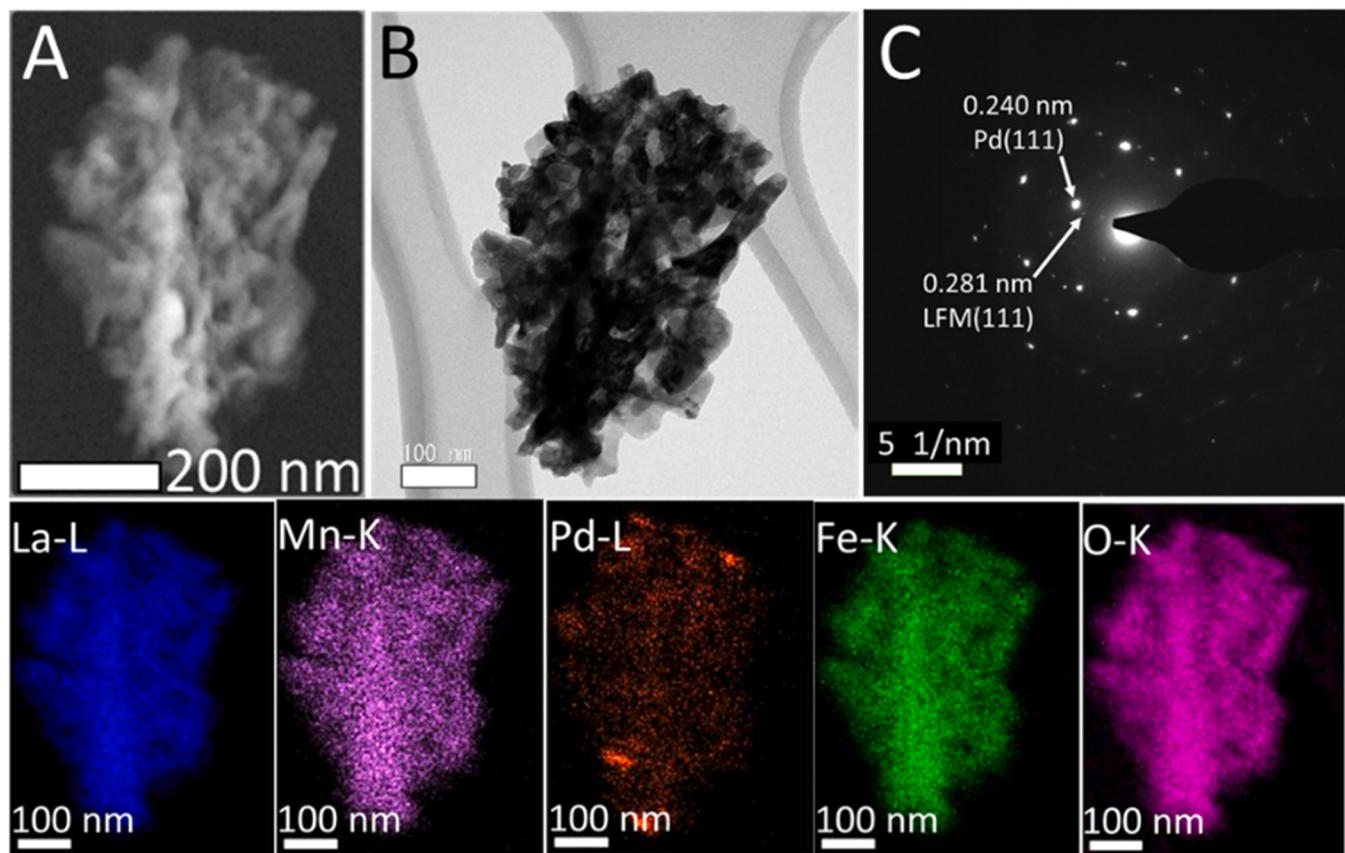


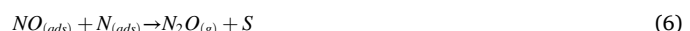
Fig. 2. TEM analysis of LaPd0.02IM after initial calcination at 600 °C. HAADF image, bright field overview image and SAED pattern are shown in panels A, B and C, respectively. In the bottom panels, EDX maps of relevant elements are shown. (La-L blue, Mn-K lilac, Pd-L red, Fe-K green and O-K purple).

600 °C. Under wet condition, the CO conversion reaches 100% at around 500 °C. The incomplete NO conversion in the presence of water at high temperatures is due to the consumption of CO in the parallel water gas shift reaction. Also other works related this effect to the lack of reduction agent in the system [42]. In the line of our chosen experimental conditions, we propose also an inhibitory effect of H₂O at higher concentrations. A slightly shifted onset temperature toward higher temperature under wet conditions compared to dry conditions indicates this effect for pure LFM. On all Pd-doped and Pd-impregnated samples a distinct promotional effect of Pd relative to pure LFM is observed under both wet and dry condition. The presence of water promotes the NO conversion on the Pd-containing catalysts and this promotion is especially prominent for the impregnated catalysts at low reaction temperatures. We emphasize that the production of small amounts of NH₃ (accompanied by an almost simultaneous decrease in N₂O concentration) is an exclusive feature of the measurements under wet conditions. Also according to these results, the enhanced NO reduction kinetics at the Pd-perovskite interface is very pronounced with respect to 2 wt% Pd/Al₂O₃ as a reference catalyst.

To interpret the catalytic data and temperature-programmed adsorption results in the next section, we below compile the representative set of previously literature-reported elementary reaction steps including reactant adsorption, reaction of intermediates and product desorption. There is a general agreement regarding the contribution of a Langmuir-Hinshelwood type of NO + CO reaction mechanism, and within this mechanism there are different mechanistic pathways conceivable for formation of various intermediates and final products, depending on the operating conditions.

The reaction mechanism is in any case a sequential reaction, initiated by (partial) dissociation of adsorbed NO and followed by CO scavenging of co-adsorbed oxygen, which would otherwise poison the surface for

further adsorption and reaction. In each equation, S refers to step-specific catalytically active sites, but not all of them necessarily refer to the same site type and location. The following elementary reaction steps (Eqs. (1)–(7)) can occur both under dry and wet conditions [31,32, 34].



In the presence of water, the water gas shift reaction (Eqs. (8)–(12)) needs to be considered [32].



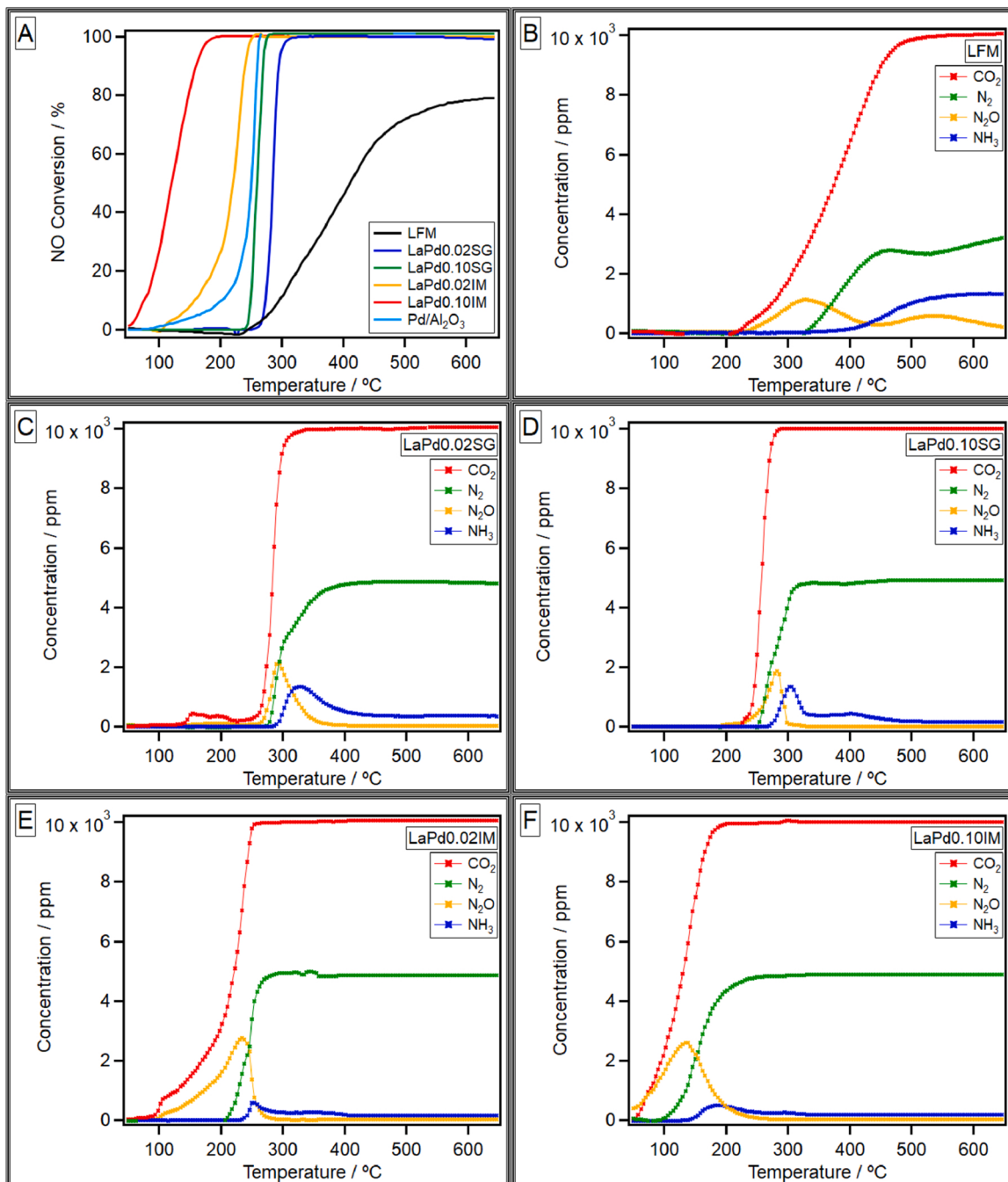


Fig. 3. Comparison of NO conversion (Panel A) and product distribution (panels B-F) during the reaction of $\text{NO} + \text{CO} + \text{H}_2\text{O}$ over the Pd-perovskite and the Pd/Al₂O₃ catalyst as indicated. Total gas flow rate: 200 mL min^{-1} with a composition of $(\text{CO}:\text{NO}:\text{H}_2\text{O}:\text{He} = 1:1:5:93)$ of the inlet flow. Heating ramp: $2 \text{ }^\circ\text{C min}^{-1}$ between $50 \text{ }^\circ\text{C}$ and $650 \text{ }^\circ\text{C}$. Sample mass: 200 mg .

However, possible NH₃ formation paths are listed in SI Eqs. (S1)–(S14).

Moreover, our ex-situ surface and bulk characterization after catalytic cycles under both dry and wet conditions indicates that catalysts undergo both structural and chemical changes to oxygen deficient structures (SI Sections B and D). In addition to purely Langmuir-Hinshelwood-type surface reaction steps related to adsorbed species from the gas phase, other, Mars-van Krevelen type reaction steps related to participation of reactive lattice oxygen need to be considered as well. Contribution of lattice oxygen in oxidation of CO and subsequent adsorption and dissociation of NO and H₂O at reductively produced oxygen vacancies (Eqs. (13)–(15)) may significantly affect the overall

catalyst performance. As it will be shown in our steady state kinetic experiments (Section 3.4), the ease of CO oxidation at the reducible Pd-support phase boundary leads to reduction of the steady state CO coverage on Pd, therefore enhancing the dissociative NO adsorption during catalysis [43].



We used H₂-TPR (as a common reference method) and CO-TPR to

compare the catalysts' reducibility and ability to produce oxygen vacancies, and subsequently tested their abilities to adsorb and dissociate NO on the produced oxygen vacancies. These experiments provide deeper mechanistic information on Eqs. (13) and (14) elementary steps.

3.3. Assessing the redox properties of the catalysts under reduction and $deNO_x$ reaction conditions

3.3.1. Reactivity of the catalysts after pre-reduction in hydrogen

3.3.1.1. Reduction profiles in hydrogen. Fig. 4 shows the temperature-programmed H_2 adsorption profiles for LFM (Panel A), LaPd0.02SG (Panel B), LaPd0.10SG (Panel C), LaPd0.02IM (Panel D), LaPd0.1IM (Panel E) and 2 wt% Pd/ Al_2O_3 (Panel F) after pre-oxidation in flowing O_2 using an initial H_2 pressure of 125 mbar. Temperature program: heating from room temperature to 700 °C (10 °C min^{-1} / full lines), followed by an isothermal period at the maximum temperature (at 700 °C for 10 min / full line) and a cooling phase (10 °C min^{-1} / broken line). The integral H_2 uptake (black) is scaled on the left axis, while the time-dependent first derivative of the H_2 uptake (molar uptake rate, blue) is scaled on the right axis.

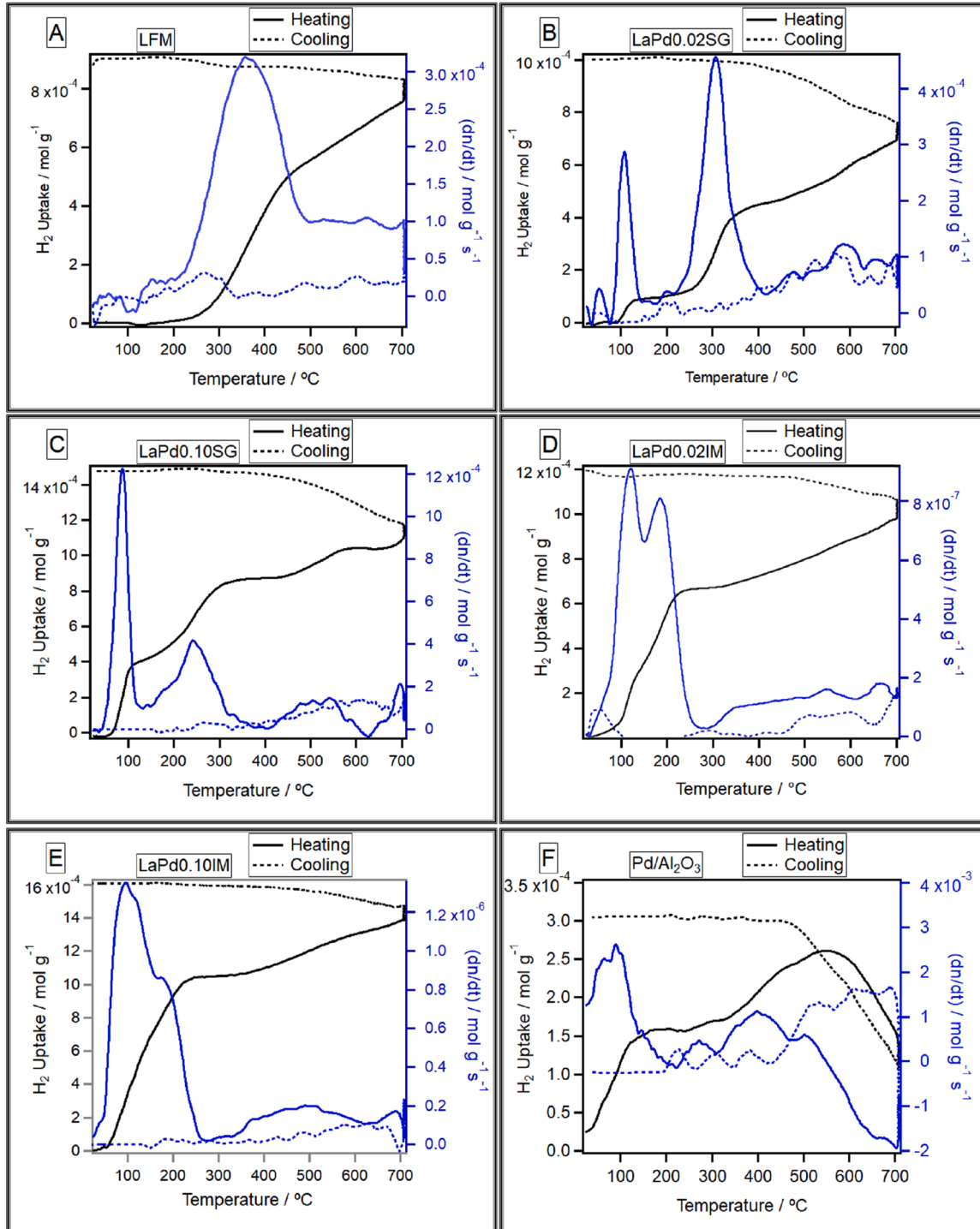


Fig. 4. Static temperature-programmed H_2 -reduction on LFM (Panel A), LaPd0.02SG (Panel B), LaPd0.10SG (Panel C), LaPd0.02IM (Panel D), LaPd0.1IM (Panel E) and 2 wt% Pd/ Al_2O_3 (Panel F) after pre-oxidation in flowing O_2 using an initial H_2 pressure of 125 mbar. Temperature program: heating from room temperature to 700 °C (10 °C min^{-1} / full lines), followed by an isothermal period at the maximum temperature (at 700 °C for 10 min / full line) and a cooling phase (10 °C min^{-1} / broken line). The integral H_2 uptake (black) is scaled on the left axis, while the time-dependent first derivative of the H_2 uptake (molar uptake rate, blue) is scaled on the right axis.

(Panel B), LaPd0.1SG (Panel C), LaPd0.02IM (Panel D), LaPd0.1IM (Panel E) and 2 wt% Pd/Al₂O₃ (Panel F). The black traces show the integral H₂ uptake of the catalysts as a function of temperature during the experiment, and the blue traces its time-dependent first derivative, i.e., the uptake rate. We use the latter to highlight the H₂ consumption onset temperatures. The H₂ uptake/uptake rate profiles during the cooling phase of the H₂-TPR are shown as broken lines. H₂ adsorption at room temperature (cf. SI, Section F, Table S2) is very small compared to the overall integral H₂ uptake. The onset temperature for the major H₂ uptake on LFM is about 260 °C, the uptake rate peaks at 350 °C and saturates at ~500 °C, suggesting a diffusion-controlled reduction mechanism beyond 500 °C. The reduction process continues isothermally at 700 °C and it almost ceases during cooling. The maximum amount of surface adsorption sites for H₂ on LFM was estimated as described in ref. [23], assuming that one H atom adsorbs on one surface unit cell of cubic LFM (area containing one La atom). This estimation yields about 5.2×10^{18} adsorption sites for the chosen sample amount of 60 mg LFM with a BET area of 12.8 m²g⁻¹ and a total overall H₂ uptake of $\sim 5.3 \times 10^{-5}$ mol H₂ or 3.2×10^{19} H₂ molecules (mass normalized: 8.8×10^{-4} mol g⁻¹), corresponding to 6 monolayers (mL) H₂ or 12 mL H(ads). Based on ref. [42], this indicates partial bulk reduction. Already the onset of the H₂ consumption temperature for the Pd incorporated samples is much lower compared to undoped LFM, indicating that Pd incorporation into LFM considerably improves the H₂ activation and reduction kinetics [37]. This trend is more pronounced for the impregnated samples, i.e., both the bulk incorporation of, and the surface doping with Pd clearly promote the reducibility of LFM because of improved H₂ activation. Although the features appear very broad and partially overlapping, we dare to assign the first uptake peak at around 100 °C to the reduction of Pd species at the surface (most likely toward Pd⁰), as this feature appears to scale with the availability of surface Pd (largest for LaPd0.1IM). If we assume all initial Pd in the impregnated samples as PdO species, a total number of PdO species in LaPd0.02IM and LaPd0.1IM catalysts of 8.18×10^{-5} mol g⁻¹ and 4.04×10^{-4} mol g⁻¹, respectively, would result. As based on the reduction kinetics, one mole H₂ is required for the reduction of one mole PdO, these numbers perfectly match the ratio of the uptake steps at around 100 °C. Consequently, we assign the second uptake peak to the reduction of the Pd-near LFM support regions. A shift of this peak to lower temperatures on all samples is prevalent, but this effect is clearly stronger on LaPd0.02IM and LaPd0.1IM. We suggest an improved synergy between the impregnated surface Pd particles on LaPd0.02IM and LaPd0.1IM and the perovskite. We speculate that this also translates to the higher observed reactivity in the reduction of NO by CO (cf. Section 3.2). Dissociation of hydrogen on the surface of better dispersed, more interface-active metallic Pd particles and an associated promoted spillover to the support is a possible explanation for this enhanced synergy effect [41,44, 45]. Although we observe partial overlap of the reduction peaks of perovskite and PdO, our observations suggest that the PdO particles in LaPd0.02IM and LaPd0.1IM are reduced at slightly higher temperatures (100 °C and 120 °C for LaPd0.1IM and LaPd0.02IM, respectively) compared to PdO on LaPd0.1SG (90 °C). Taking all indications from TEM and TPR together, both Pd impregnated samples exhibit a larger and/or more active Pd-LFM interface. Vice versa, the Pd over-doping in LaPd0.1SG creates larger PdO particles with less or less active interface. Consequently, these PdO particles are reduced independently of the perovskite at somewhat lower temperatures. We are, thus, able to prepare differently reactive/ abundant Pd-perovskite interfaces by impregnation and Pd over-doping, exhibiting different activation kinetics. In the case of Pd/Al₂O₃, the major H₂ uptake starts at around 50 °C and after intermediate saturation, starts again around 350 °C. Negative H₂ uptakes at temperatures higher than 550 °C could be due to desorption of H₂ from PdH_x phases, which are formed already at low temperatures [46]. Finally, at the end of H₂-TPR, the integral H₂ uptake on this sample is much lower than for the perovskite samples.

3.3.1.2. NO reduction capacity of the hydrogen - pre-reduced catalysts (NO-TPO). The reactivity of the reduced samples toward NO reduction after H₂-TPR is shown in Fig. 5 for LFM (Panel A), LaPd0.02SG (Panel B), LaPd0.1SG (Panel C), LaPd0.02IM (Panel D), LaPd0.1IM (Panel E) and 2 wt% Pd/Al₂O₃ (Panel F). Quantitative results are summarized in Section F, Table S2 of the SI. All reduced samples were active for NO adsorption/dissociation (Eqs. (1) and (3)) and featured the same onset temperature for NO reduction (~ 150 °C). Neither Pd doping nor impregnation significantly influence the onset temperature of the perovskite samples. N₂O and N₂ are the only reaction products and the lack of oxygen at the reactor outlet indicates that all the oxygen derived from the NO dissociation is dissolved within the catalyst bulk, quenching oxygen vacancies. The results indicate that NO dissociation also occurs on the pure perovskite and that N₂O is the first product of NO reduction for all catalysts. As the temperature increases above 250 °C, N₂ starts to form on the perovskite catalysts. According to Eq. (6), the formation of N₂O is a function of the available temperature range with simultaneous population of the surface with both dissociated and undissociated NO species [47]. The N₂O concentration peaks exhibit a maximum between 300 °C and 400 °C. As pumping effects are compensated by normalization to the Ar MS signal, the decrease of N₂O corresponds to its consumption during Eq. (7) to form N₂. These results indicate that N₂O is a gas phase intermediate between NO and N₂, which can readorb and react further to N₂ on the catalyst surface. According to Eqs. (3), (4) and (7), the selectivity of N₂ is determined by the NO/N₂O dissociation and/or N atom recombination steps. Hence, the high selectivity to N₂ can be attributed to the low energy barrier for NO/N₂O dissociation and N atom recombination [47]. Thus, Fig. 5 supports the view that the Pd surface and/or phase boundary to the perovskite improves the N₂ formation kinetics based on shifting its production onset temperature to lower temperatures. On the Pd/Al₂O₃ catalyst, the NO reduction starts at relatively higher temperatures and the integral reduced NO is lower compared to the perovskite samples.

3.3.2. Reactivity of the catalysts after pre-reduction in CO

3.3.2.1. Reduction capacity in CO. To analyze the oxidation of CO by lattice oxygen (Eq. (13)) and to assess the catalytic activity of the samples in the process of NO reduction by CO we pre-tested the reducibility of the samples in quasi-static temperature-programmed CO experiments. After room temperature CO adsorption (quantitative analysis given in SI, Section F, Table S3), CO-TPR profiles were collected for LFM, LaPd0.02SG, LaPd0.1SG, LaPd0.02IM, LaPd0.1IM and Pd/Al₂O₃ (Section F, Fig. S18). Upon temperature increase, adsorbed CO reacts with oxygen released from the catalyst toward CO₂, thereby reducing the catalyst. During the isothermal period, the CO reduction rate becomes very low, especially for samples with a higher amount of Pd, and it stops during the cooling phase. We show the integral CO uptake (in mol g⁻¹) for each sample in Fig. 6. Unlike the lower H₂-TPR onset temperature, CO reduction starts around 150 °C for the Pd-impregnated samples, at 200 °C for LaPd0.1SG and for LFM and LaPd0.02SG at about 250 °C. In comparison to pure LFM, the presence of Pd does not change the total CO uptake or its kinetics for LaPd0.02SG sample significantly. For the other samples (especially LaPd0.1IM) its promotion effects are pronounced. Samples with more Pd (especially at the surface) are clearly capable of reducing more CO. Reduction of PdO particles on the catalyst surface already occurs at room temperature in CO atmosphere during 10 min room temperature adsorption and during the equilibration time of the QMS signals before CO-TPR (about 1 h as described in the experimental section). As PdO reduction by CO especially at room temperature is immediate and limited, as reported before [48,49], in quantitative calculations we have considered only the CO adsorption within the first 10 min. In accordance with previous studies on the CO adsorption on Pd-Ce/Al₂O₃ catalysts, which assume an Pd-metal covered PdO core, which is progressively reduced [50], we postulate a similar chemical

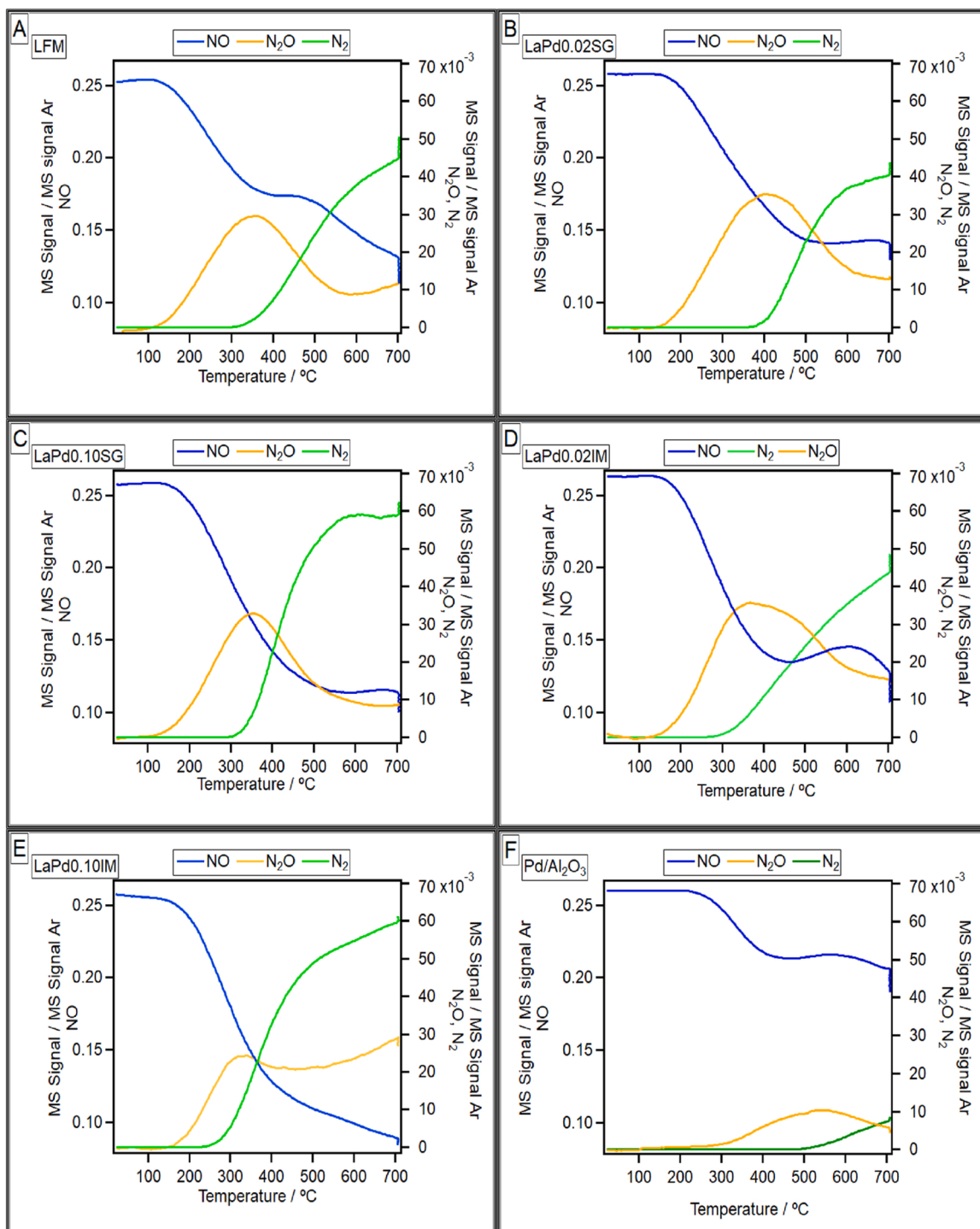


Fig. 5. Quasi-static temperature-programmed oxidation of NO on hydrogen pre-reduced LFM (Panel A), LaPd0.02SG (Panel B), LaPd0.1SG (Panel C), LaPd0.02IM (Panel D), LaPd0.1IM (Panel E) and 2 wt% Pd/Al₂O₃ (Panel F). Ar-normalized MS signals of NO (*m/z* = 30, blue), N₂ (*m/z* = 28, green) and N₂O (*m/z* = 44, orange) are shown. The samples were heated in a NO:Ar (initially 1:4) mixture at a rate of 10 °C min⁻¹ between 25 °C and 700 °C including an isothermal period at 700 °C for 10 min.

meaningful scenario here. Comparing the improved kinetic reduction trend (i.e., lower onset temperatures) of Pd-impregnated samples with the Pd-doped ones, this observation may again be linked to the existence of a larger phase boundary on the Pd-impregnated samples, promoting spillover of adsorbed CO on Pd to the perovskite. The comparatively steep increase in CO uptake for LaPd0.1SG at relatively high temperature (250–400 °C) is interpreted in terms of a rather “support-independent” reduction of the Pd particle bulk structure as a possible result

of the lower extent of phase boundary. According to Fig. 6, Pd promotes the CO reduction kinetics of both the pure and Pd-doped LFM samples and improves the total quantitative CO reduction capacity of the catalysts (cf. SI, Section F, Table S3).

3.3.2.2. NO reduction capacity of the CO – pre-reduced catalysts. Fig. 7 shows the NO reduction capability of the CO reduced samples for LFM (Panel A), LaPd0.02SG (Panel B), LaPd0.1SG (Panel C), LaPd0.02IM

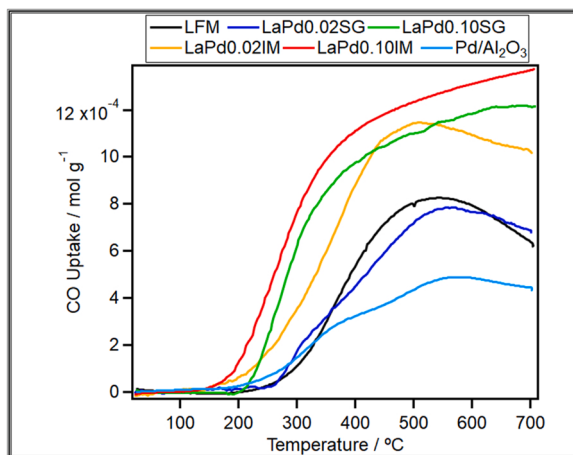


Fig. 6. Quasi-static CO-TPR profile on LFM (black), LaPd0.02SG (blue), LaPd0.10SG (green), LaPd0.02IM (purple), LaPd0.10IM (red) and 2 wt% Pd/Al₂O₃ (aqua) catalysts after pre-oxidation in flowing O₂. The samples were heated in a 125 mbar CO:Ar (initially 1:4) mixture at a rate of 10 °C min⁻¹ starting at RT.

(Panel D), LaPd0.1IM (Panel E) and Pd/Al₂O₃ (Panel F). All samples feature NO reduction and simultaneous N₂O and CO₂ formation, while N₂ is formed at higher temperatures. Formation of CO₂ along with N₂O is confirmed by evaluating the entire set of QMS signals including *m/z* = 22 for CO₂²⁺. In the case of the perovskite samples, N₂ formation onset temperatures (in analogy to the H₂-prereduced NO-TPO results) and the NO reduction kinetics (unlike the H₂-prereduced NO-TPO) exhibit a pronounced sample- and Pd-dopant/impregnation dependency. For LFM and lower Pd loadings (LaPd0.02SG and LaPd0.02IM), the onset temperature for NO reduction is higher as compared to the respective hydrogen pre-reduced samples. We attribute this to an inhibitory effect of carbonaceous species (especially amorphous carbon, confirmed by TEM, see Section 3.1.) on NO adsorption and activation on the catalysts. This is further confirmed by the reduced room temperature NO adsorption (cf. SI, Section F, Table S3) on these samples in comparison to the respective hydrogen pre-reduced samples. The NO reduction is kinetically different in the presence of adsorbed carbonaceous species and by increasing the Pd content of the samples, the onset temperature for NO reduction shifts to lower temperatures. As the NO reduction onset on LaPd0.1IM and its room temperature adsorption is similar to the H₂-reduced one, we conclude that adsorbed carbonaceous species do not block active NO dissociation sites at the phase boundary. In addition, oxygen resulting from NO dissociation at the phase boundary can effectively be consumed by CO adsorbed on metallic Pd and re-supplies reduction sites at the phase boundary sites active for NO adsorption and dissociation. According to the quantitative evaluation of the total amount of converted NO (Tables S2 and S3 in SI), it can be concluded that CO pre-reduced pure LFM and sol-gel samples exhibit a lower capacity for NO reduction than the respective hydrogen pre-reduced samples. This could again be due to the lower concentration of bulk oxygen vacancies and/or differences regarding the inhibitory effect of surface-adsorbed carbon species. For LaPd0.02IM and LaPd0.1IM, the carbon monoxide – pre-reduced samples exhibit almost equal or more NO consumption than their hydrogen – pre-reduced counterparts. However, our calculation for complete oxygen balance after a full redox cycle including final quantitative re-oxidation in O₂ (CO/H₂-TPR, NO-TPO, TPD, O₂-TPO, quantitative results are summarized in Tables S2 and S3) indicates that the amount of vacancies that cannot be quenched by NO was comparably high in the CO-pre-reduced samples. These results altogether indicate that in addition to oxygen vacancies, carbonaceous species also contribute to the overall NO reduction, as observed for a similar situation for the CO₂ production during NO reduction on reduced ceria-based catalysts [51]. Again,

according to results of Panel F, the Pd/Al₂O₃ catalyst kinetically and quantitatively is less active for NO reduction than the perovskite samples.

In summary, the temperature-programmed experiments yield the following information: CO oxidation by lattice oxygen is promoted at the Pd – perovskite phase boundary, which provides new sites for NO adsorption and dissociation. The inhibitory effects for NO reduction and poisoning of CO are reduced at the phase boundary. The phase boundary effectively consumes oxygen derived from NO dissociation in oxidation of adsorbed CO. N₂ recombination is also promoted at the phase boundary.

3.4. Steady state reaction kinetics study

In order to obtain more information on phase boundary effects and to clarify the effect of water on the product distribution, we have performed steady state kinetic experiments at varying NO, CO and H₂O concentrations. To obtain reaction orders, we fitted experimental rates to power law equations, $r_i = k_i C_{NO}^\alpha C_{CO}^\beta C_{H_2O}^\gamma$ where α , β , γ denote the reaction orders. To determine the reaction order for each reactant, a constant concentration of the other reactants was used while varying the target reactant concentration. In each experiment, we adjusted variations in the feed composition by changing the He flow rates and the bubbling water temperature to achieve a constant total flow rate of 200 mL min⁻¹.

In Fig. 8, panels A and B show representatively the reaction rates for CO₂, N₂, N₂O, NH₃ formation and total NO consumption over the LaPd0.10IM catalyst at 250 °C as a function of the concentration of CO and NO, respectively. Full lines are drawn as a guide to the eye. As the CO concentration increases, the rate of NO consumption and subsequently the CO₂, N₂O and N₂ production increases. Significant amounts of NH₃ are produced only at higher CO concentration. The comparably strong increase in reaction rate by increasing the CO concentration indicates that CO adsorption is rate determining step at lower CO concentration. Consumption of NO and subsequently, the formation of N₂O and N₂ rates decrease again after passing a maximum at a CO concentration of about 0.18 mol m⁻³, where the CO₂ production rate saturates. In Panel B, with the exception of NH₃, which shows an increase and then a decreasing behavior, all the rates increase with increasing NO concentration. The appearance of the characteristic rate maxima in NO reduction rates in Panel A, which is a clear hint to the inversion of reaction order with respect to the CO concentration, indicates a competitive adsorption of NO and CO on catalyst surface. As it occurs at C_{NO}/C_{CO} > 1, stronger adsorption of CO relative to NO is concluded [51,52] and continuously enhanced rates with respect to increasing C_{NO} (Panel B) support this claim. As shown in Panel C, the reaction orders of NO, CO₂, N₂ and N₂O rates derived from varying NO concentration are altogether positive. In the case of the NO+CO+H₂O reaction, positive reaction order values for NO refers to relatively weaker adsorption of NO compared to adsorption of CO, and the dissociation of NO will become energetically less favorable on the increasingly CO-poisoned catalyst surface [53,54].

As NH₃ rates show a change in reaction order for NO under these experimental conditions, we have not fitted its data. The key question is, why – despite the decrease of NO conversion rates and subsequently the N₂ and N₂O rates – CO₂ production does not decrease during increasing CO concentration. We tentatively assign this to the effect of H₂O and consumption of CO in the parallel occurring water gas shift reaction. The resulting hydrogen, in the presence of excess CO, leads to the concomitant formation of NH₃. For further clarification, we have repeated this experiment for LaPd0.10IM in the absence of water (SI, Section E, and Fig. S16). Here, the reaction order with respect to CO changes at higher CO concentrations and poisoning effects occur also for CO₂ production. In addition, we observe a shift of the maximum rate positions to lower CO concentrations in absence of water. Konsolakis et al. used such an observation to interpret the promotion of Pd/YSZ by alkali metals for

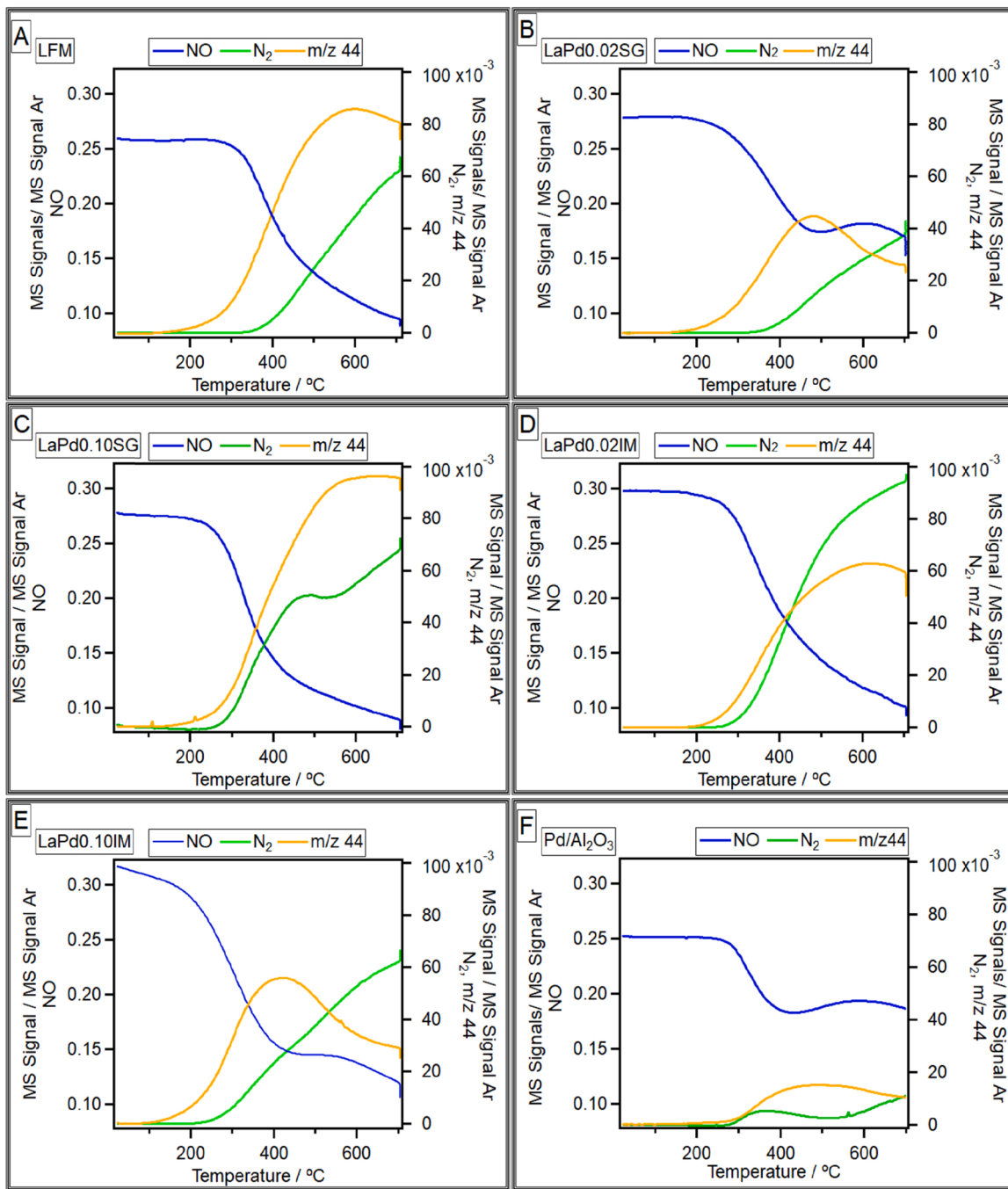


Fig. 7. Quasi-static NO-TPO profiles on LFM (Panel A), LaPd0.02SG (Panel B), LaPd0.10SG (Panel C), LaPd0.02IM (Panel D), LaPd0.10IM (Panel E) and 2 wt% Pd/Al₂O₃ (Panel F) after carbon monoxide pre-reduction. Ar-normalized MS signals of NO ($m/z = 30$, blue), N₂ ($m/z = 28$, green) and N₂O/CO₂ ($m/z = 44$, orange) are shown. The samples were heated in a NO:Ar (initially 1:4) mixture at a rate of $10^{\circ}\text{C min}^{-1}$ between 25°C and 700°C . Subsequently, the sample was heated isothermally at 700°C for 10 min.

more effective adsorption of NO [52]. Our results indicate that the observed promotion effect of H₂O (Section 3.2) and Section E in SI) could be due to the consumption of excess CO via the parallel water gas shift reaction and the corresponding attenuation of its poisoning effects in the NO reduction reaction. In this line of argumentation, comparison of LaPd0.02SG and LaPd0.10IM catalysts is useful for investigating the promotional origin of the phase boundary during the reaction. According to Figs. S16 and S17, the rate maximum position and the obtained reaction orders with respect to CO in its prohibiting concentration range (and also the reaction orders for NO) clearly indicate the attenuation of the inhibitory effect of CO for the catalysts with a larger amount of phase

boundary sites. This is in line with our conclusions from volumetric adsorption experiments in Section 3.3. Obviously, CO poisoning of active phase boundary sites is less efficient. Vice versa, based on the interpretation in ref. [52], a strongly negative CO reaction order observed for LaPd0.02SG (which is associated with a strongly positive order for NO) can be related to dominant adsorption of CO vs. NO and more efficient active site poisoning for LaPd0.02SG. Reaction orders for each component derived from the H₂O concentration change are shown in Panel D. All the components exhibit a relatively weak or missing dependency on the concentration of H₂O. CO₂ and NH₃ rates exhibit positive, and N₂, N₂O and NO negative reaction orders. Our results are in

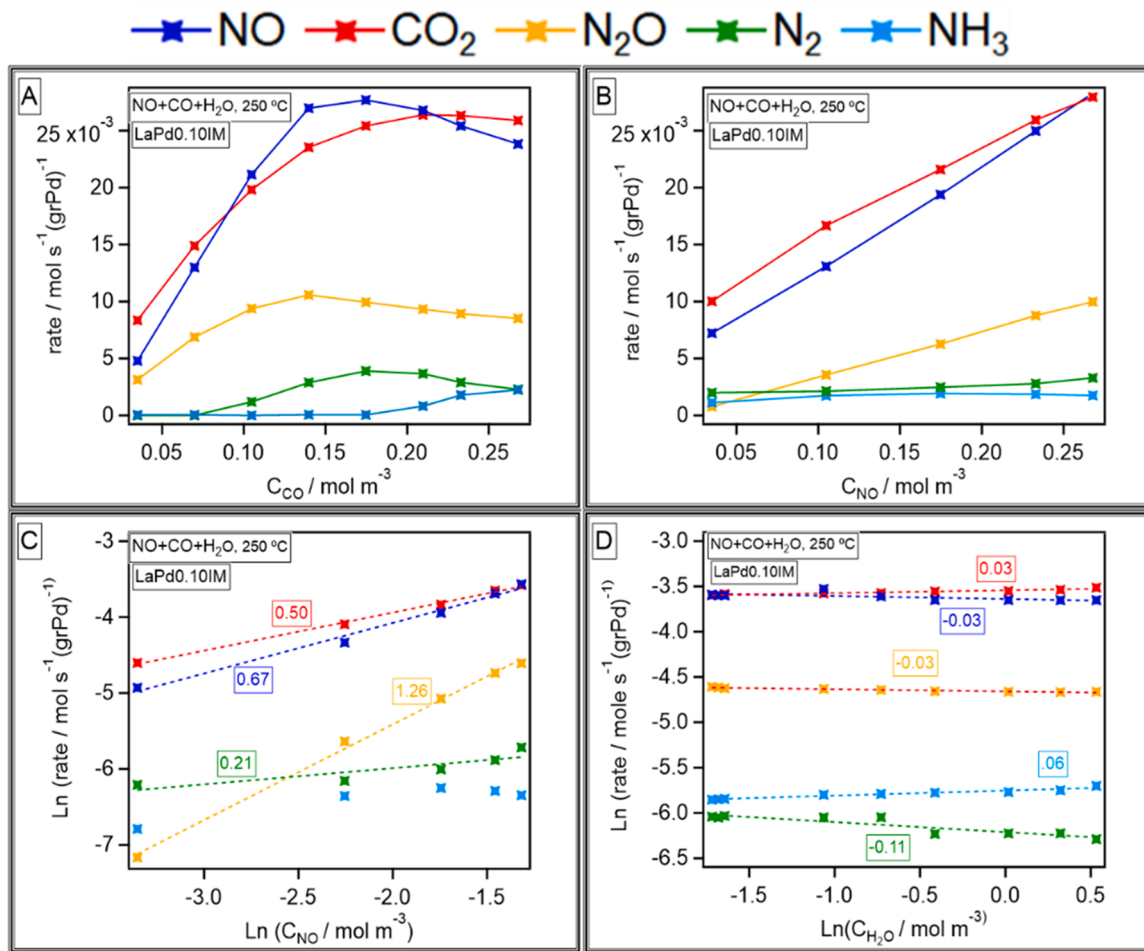


Fig. 8. Reaction rates at 250 °C as a function of CO (Panel A), NO (Panels B and C), and H₂O (Panel D) concentration. The reaction orders for each component with respect to NO and H₂O concentration are shown in the boxes. The dotted lines are the fitted linear equations for each component after logarithmization of the rate equation. Operating conditions: (Panel A) C_{NO} = 0.23 mol m⁻³, C_{H2O} = 0.57 mol m⁻³; (Panels B and C) C_{CO} = 0.23 mol m⁻³, C_{H2O} = 0.57 mol m⁻³; (Panel D) C_{CO} = 0.23 mol m⁻³, C_{NO} = 0.23 mol m⁻³. Total flow rate 200 mL min⁻¹. NO/CO conversion for all the experiments was kept below 20%.

good accordance with [55] and the observed discrepancy regarding the sign of reaction orders for the NO rate is likely related to the CO-rich operating conditions, for which an increase in H₂O concentration could lead to an increase in NO reduction with enhanced selectivity to NH₃. Possible explanations for suppression of the NO conversion at high H₂O concentrations could be partial blocking of NO adsorption and dissociation sites by H₂O. Our temperature-programmed catalytic results (not shown here) at different H₂O concentrations (2.5% and 5% H₂O), further support the obtained small negative order of the NO consumption rate with respect to H₂O concentration. According to these results, the decrease of the N₂ and N₂O production rates together with decreasing NO reduction rates shows that they depend strongly on NO adsorption/dissociation, as compared to NH₃ production rates, which show a continuous increase with increasing CO and H₂O concentrations. The observed maximum feature for the NH₃ concentration in the temperature-programmed catalytic results (Fig. 3) could be due to its decomposition at high temperatures [56] or due to a decrease in CO coverage of active sites with increasing temperature which is confirmed by our results shown in Fig. 9. Of course, increased NO dissociation and subsequently, an increase in the propensity for N₂ formation, can also account for the decrease in NH₃ selectivity with increasing temperature. Adams et al. reported that an increase in NO adsorption / dissociation ability of a catalyst leads to a decrease in NH₃ production [55]. Table 2 summarizes the obtained reaction orders for NO and CO in the concentration ranges given in Fig. 8.

To further investigate the effect of temperature, the effect of different

levels of conversion and also the effect of presence and absence of H₂O on reaction performance and product selectivity, we performed another set of steady state kinetic experiments at varying NO and CO concentrations. In these experiments, conversion values are high, therefore the reactor was operated under differential conditions, and we used different amounts of catalyst to achieve variable conversions. Fig. 9, panels A-F show the isothermal steady state conversions of NO/CO (left) and the respective product selectivity (right) over the LaPd0.10IM catalyst as a function of CO concentration under dry vs. wet conditions. At 180 °C and under dry conditions (Panels A and B), the NO conversion increases with increasing CO concentration, which is accompanied by a slight decrease in CO conversion, and then decreases again after reaching a maximum around C_{CO} = 0.17 mol m⁻³, indicating competitive adsorption of NO and CO. The N₂ selectivity increases with increasing NO conversion, whereby the N₂O selectivity shows an opposite behavior. According to Eqs. (4) and (6), this behavior is expected because the increase in NO conversion results from an increase in the dissociation rate of NO, which is associated with an enhanced amount of surface-adsorbed N species and N₂ production probability. NO and CO conversion levels and ranges increase at 300 °C (Panels C and D). At 300 °C, the decrease in NO and CO conversions due to poisoning effects of CO is shifted to higher CO concentrations. As can be expected, the isothermal CO coverage on the catalyst surface will increase with increasing concentration, thus re-establishing the poisoning effect. It is worth to mention, that the maximum NO conversion position is not related to a distinct NO or CO concentration, but it is rather a

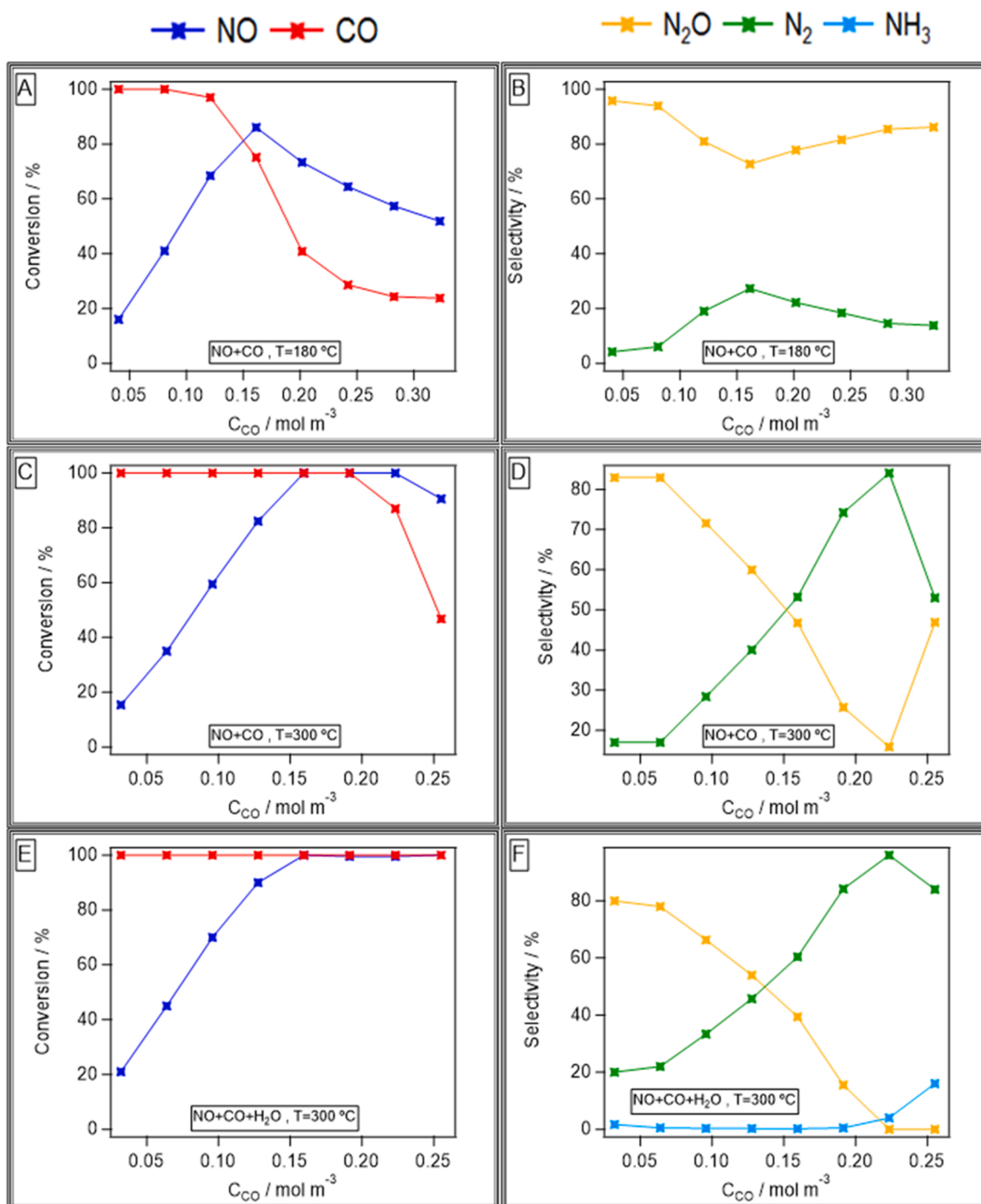


Fig. 9. NO/CO conversion and product selectivity as a function of CO concentration on LaPd0.10IM at constant temperature under dry vs. wet conditions. The total flow rate was 200 mL min^{-1} , $C_{\text{NO}} = 0.26 / 0.21 \text{ mol m}^{-3}$ (depending on temperature) and $C_{\text{H}_2\text{O}} = 0.66 / 0.54 \text{ mol m}^{-3}$. Panels A and B: conversion and selectivity at 180°C under dry conditions; Panels C and D: conversion and selectivity at 300°C under dry conditions; Panels E and F: conversion and selectivity at 300°C under wet conditions. Lines are drawn as a guide to the eye.

Table 2

Reaction orders of NO and CO under wet and dry conditions over LaPd0.02SG and LaPd0.10IM for NO reaction and CO_2 formation.

Rate	α			β			γ		
	LaPd0.02SG-dry	LaPd0.10IM-dry	LaPd0.10IM-wet	LaPd0.02SG-dry	LaPd0.10IM-dry	LaPd0.10IM-wet	LaPd0.02SG-dry	LaPd0.10IM-dry	LaPd0.11MO-wet
$-\text{r}_{\text{NO}}$	1.01	0.68	0.67	-0.66	-0.6	-0.47	—	—	-0.03
r_{CO_2}	0.99	0.53	0.5	-0.58	-0.45	0	—	—	0.03

function of C_{NO}/C_{CO} ratio. The N_2O and N_2 selectivity trends are similar to 180 °C and N_2 is the major product, which is due to the high NO conversion at 300 °C. However, a sudden increase in N_2O selectivity (Panel D), which goes along with a decrease in NO conversion, indicates that the simultaneous presence of adsorbed N and NO species on the catalyst surface is necessary for the formation of N_2O , regardless of reaction temperature. In the presence of water at 300 °C, a corresponding drop in conversion is absent even at high CO concentration. Again, these results indicate that presence of water helps to “de-poison” the catalyst surface with respect to adsorbed CO species, which counteract efficient adsorption and reaction of NO. We note that the presence of water also helps to increase the N_2 selectivity at lower CO concentrations. Moreover, NH_3 production increases again with increasing CO concentration, indicating the operation of a CO-related NH_3 production pathway.

In Fig. 10, Panels A and B we show the steady state conversions of NO/CO and the product selectivity over the LaPd0.10IM catalyst as a function of NO concentration at 300 °C in presence of 0.52 mol m⁻³ H_2O . CO conversion increases with increasing NO concentration and reaches 100% at $P_{NO} = 0.8$ kPa. In addition to the discussed competitive adsorption effects, these results reveal that the catalyst is considerably more active toward the NO + CO as compared to the CO + H_2O reaction. Only under CO rich conditions considerable amounts of NH_3 can be produced, but under nearly stoichiometric conditions, the desired harmless N_2 is the main product.

As can be deduced from the discussion above, the NH_3 formation rate exhibits a negative order dependency on the NO concentration and a positive order dependency on CO and H_2O . According to both experimental evidence and literature reports [23,32,33,55], NH_3 formation could proceed through all proposed three pathways starting from adsorbed NO, N and NCO species as a consequence of the CO- H_2O interaction and at the same time enough H(ads) to promote the hydrogenation route. Fig. 3 shows that NH_3 is in any case the product formed at the highest temperature of all products and at/around the temperature where N_2O decreases, NH_3 is starting off. As a high temperature causes an increased abundance of N(ads), the NCO pathway and also direct hydrogenation of N(ads) are more likely pathways for NH_3 formation.

Summarizing the experimental results, LaPd0.10IM exhibits the highest activity at any reaction temperature, because it exhibits a maximum number of Pd^0 -LFM phase boundary sites, which more effectively convert CO and reduce its poisoning effect for NO adsorption, dissociation and reduction. LaPd0.02IM shows an analogous reactivity pattern with less overall activity. We infer the same type of active phase boundary sites, but a reduced number in LaPd0.02IM due to the lower

Pd content. Enhanced NO dissociation activity for both impregnated catalysts leads to an increase in N_2 selectivity. LaPd0.1SG performs hardly better than LaPd0.02SG. This is due to the poor Pd -dispersion and the apparent absence of Pd^0 on LaPd0.1SG, indicating only a small rate contribution of phase boundary sites, if at all. Generally, a much steeper conversion increase for the Pd -doped catalysts relative to pure LFM around the same onset temperature can be assigned to the enhanced activity of the Pd^{2+} -promoted LFM surface itself. Finally, pure LFM exhibits the lowest activity due to the absence both of active Pd^0 -LFM interface and Pd^{2+} -LFM lattice centers.

4. Conclusions

We are able to steer the catalytic performance and the redox chemistry of the Pd – LFM perovskite interface towards optimum NO reactivity in presence of water by following different preparation approaches. The morphology of the resulting Pd species on the surface of the perovskite strongly differs for the Pd -impregnated and Pd -doped perovskites, directly translating to different de- NO_x reactivity. While for the LaPd0.02SG sample all Pd is introduced into the perovskite (providing the highly dispersed Pd benchmark without initial Pd -perovskite interface), deliberately exceeding the Pd doping capacity of the LFM perovskite (LaPd0.1SG) introduces separately crystallized large PdO particles on the surface with an associated small amount of phase boundary and subsequently low catalytic activity. Well distributed metallic Pd and PdO species in the impregnated catalysts without Pd incorporated into the perovskite lattice represent the “only Pd -perovskite interface” benchmark. Volumetric adsorption studies and further investigation into the reaction orders showed that the strong adsorption of CO on LaPd0.02SG could rather act as an inhibitor that might hinder the facile adsorption/dissociation of NO, while the LaPd0.10IM catalyst exhibited attenuated CO poisoning effects, which additionally decreased in the presence of H_2O . Tentatively, we suggest that the optimized use of lattice oxygen for CO oxidation at the Pd -perovskite phase boundary and its replenishment from NO dissociation allows for more poisoning-resistant active sites for NO activation, and that this may represent the main promotional mechanism on the impregnated catalysts. Reaction of H and OH species derived from H_2O dissociation with adsorbed CO or other carbon containing species assists further surface clean-off. Enhanced NO reduction activity on the “de-poisoned” surface/interface leads to a pronounced increase in N_2 selectivity. According to isothermal kinetic reactant concentration variation studies, the product selectivity is a function of mostly the relative concentrations of NO and CO. Preferred production of NH_3 at

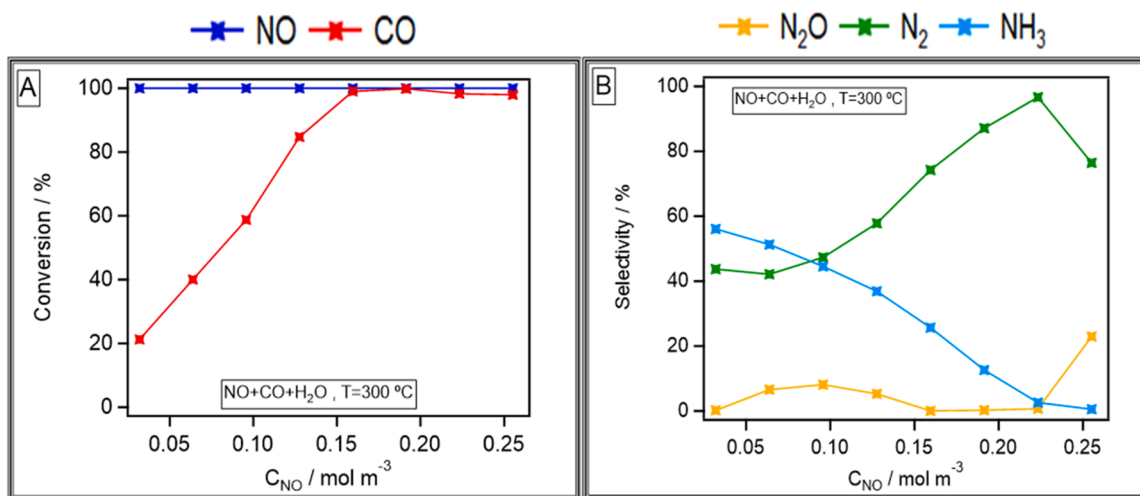


Fig. 10. NO/CO conversion (Panel A) and product selectivity (Panel B) as a function of NO concentration for LaPd0.10IM at 300 °C. Total flow rate 200 mL min⁻¹, $C_{CO} = 0.21$ mol m⁻³ and $C_{H_2O} = 0.52$ mol m⁻³.

low NO and high CO and H₂O concentrations indicates that enhanced population of water gas shift intermediates is linked to increased surface hydrogen activity and leads to increased gas phase NH₃ formation.

We exemplify the steering principle only for one particular Pd-lanthanum iron manganite interface, but beyond the proof-of-principle, generalization to similar systems will enlighten the operational principles of metal-doped perovskite systems under deNOx conditions and open up various possibilities for the knowledge-based design of perovskite materials for exhaust gas treatment. One particular parameter, that needs to be addressed in future directed studies is the potential deactivation behavior of the discussed metal-perovskite interfaces over a longer time-on-stream with respect to metal particle sintering and consequently, general structural deterioration of the metal-perovskite interface. At high enough temperature, we might also anticipate anti-segregation of already exsolved perovskite constituents under oxidizing conditions, as the synthesis of the parent perovskite can take place via a solid-state reaction of the individual oxidic components. The exact conditions to drive an exsolution/ anti-segregation cycle (which may lead to metal re-dispersion) are still a vast open field of research.

CRediT authorship contribution statement

Asghar Mohammadi: Experimental work, Manuscript draft preparation. **Ali Farzi:** Conceptualization. **Christoph Thurner:** Experimental work. **Bernhard Klötzer:** Conceptualization, Funding. **Sabine Schwarz:** Experimental work. **Johannes Bernardi:** Experimental work. **Aligholi Niaezi:** Conceptualization, Supervision. **Simon Penner:** Conceptualization, Supervision, Final manuscript preparation.

Declaration of Competing Interest

The authors declare that they have no known competing financial interests or personal relationships that could have appeared to influence the work reported in this paper.

Acknowledgments

The work was performed within the framework of the bilateral IMPULSE program Austria-Iran of the OEAD (Österreichische Austauschdienst GmbH) and is financially also supported by the special research platform “Advanced Materials” at the University of Innsbruck.

Appendix A. Supplementary material

Supplementary data associated with this article can be found in the online version at [doi:10.1016/j.apcatb.2022.121160](https://doi.org/10.1016/j.apcatb.2022.121160).

References

- [1] R.J. Farrauto, M. Deeba, S. Alerasool, Gasoline automobile catalysis and its historical journey to cleaner air, *Nat. Catal.* 2 (2019) 603–613.
- [2] C.K. Lambert, Current state of the art and future needs for automotive exhaust catalysis, *Nat. Catal.* 2 (2019) 554–557.
- [3] S. Rood, S. Eslava, A. Manigrasso, C. Bannister, Recent advances in gasoline three-way catalyst formulation: a review, *Proc. Inst. Mech. Eng. Part D J. Automob. Eng.* 234 (2020) 936–949.
- [4] B. Li, M.B. Katz, Y. Duan, X. Du, K. Zhang, L. Chen, A. Van der Ven, G.W. Graham, X. Pan, A joint theoretical and experimental study of phase equilibria and evolution in Pt-doped calcium titanate under redox conditions, *Chem. Mater.* 27 (2015) 18–28.
- [5] N. Li, A. Boréave, J.-P. Deloume, F. Gaillard, Catalytic combustion of toluene over a Sr and Fe substituted LaCoO₃ perovskite, *Solid State Ion.* 179 (2008) 1396–1400.
- [6] S. Rousseau, S. Lordinant, P. Delichere, A. Boreave, J. Deloume, P. Vernoux, La_(1-x) Sr_xCo_{1-x}Fe_yO₃ perovskites prepared by sol-gel method: characterization and relationships with catalytic properties for total oxidation of toluene, *Appl. Catal. B* 88 (2009) 438–447.
- [7] X. Zhu, K. Li, L. Neal, F. Li, Perovskites as geo-inspired oxygen storage materials for chemical looping and three-way catalysis: a perspective, *ACS Catal.* 8 (2018) 8213–8236.
- [8] M. Pena, J. Fierro, Chemical structures and performance of perovskite oxides, *Chem. Rev.* 101 (2001) 1981–2018.
- [9] A. Giannakas, A. Ladavos, P. Pomonis, Preparation, characterization and investigation of catalytic activity for NO+ CO reaction of LaMnO₃ and LaFeO₃ perovskites prepared via microemulsion method, *Appl. Catal. B* 49 (2004) 147–158.
- [10] A. Leontiou, A. Ladavos, P. Pomonis, Catalytic NO reduction with CO on La_{1-x} Sr_x (Fe³⁺/Fe²⁺) O_{3±δ} perovskite-type mixed oxides (x = 0.00, 0.15, 0.30, 0.40, 0.60, 0.70, 0.80, and 0.90), *Appl. Catal. A* 241 (2003) 133–141.
- [11] V.C. Belessi, C.N. Costa, T.V. Bakas, T. Anastasiadou, P.J. Pomonis, A. M. Efstratiou, Catalytic behavior of La-Sr-Ce-Fe-O mixed oxidic/perovskitic systems for the NO+ CO and NO+ CH₄+ O₂ (lean-NO_x) reactions, *Catal. Today* 59 (2000) 347–363.
- [12] S. Peter, E. Garbowski, V. Perrichon, M. Primet, NO reduction by CO over aluminate-supported perovskites, *Catal. Lett.* 70 (2000) 27–33.
- [13] L. Simonot, G. Maire, A comparative study of LaCoO₃, CO₃O₄ and a mix of LaCoO₃–Co₃O₄: II. Catalytic properties for the CO+ NO reaction, *Appl. Catal. B* 11 (1997) 181–191.
- [14] A. Glisenti, M. Pacella, M. Guiotto, M. Natile, P. Canu, Largely Cu-doped LaCo_{1-x} Cu_xO₃ perovskites for TWC: toward new PGM-free catalysts, *Appl. Catal. B* 180 (2016) 94–105.
- [15] B. Izadkhah, A. Niaezi, D. Salari, S. Hosseinpour, S.A. Hosseini, A. Tarjomannejad, Catalytic removal of CO and NO_x using sol-gel synthesized LaB_{0.5}Co_{0.5}O₃ (B = Cr, Mn and Cu) and LaMn_x Co_{1-x}O₃ nano-perovskites, *Korean J. Chem. Eng.* 33 (2016) 1192–1199.
- [16] B. Izadkhah, A. Niaezi, M.J. Illán-Gómez, D. Salari, A. Tarjomannejad, V. Albaladejo-Fuentes, LaBO₃ (B = Mn, Fe, Co, Ni, Cu, and Zn) Catalysts for CO+ NO Reaction, *Ind. Eng. Chem. Res.* 56 (2017) 3880–3886.
- [17] A. Tarjomannejad, A. Farzi, M.J. Gómez, A. Niaezi, D. Salari, V. Albaladejo-Fuentes, Catalytic reduction of NO by CO over LaMn_{1-x} Fe_xO₃ and La_{0.8}A_{0.2}Mn_{0.3}Fe_{0.7}O₃ (A = Sr, Cs, Ba, Ce) perovskite catalysts, *Catal. Lett.* 146 (2016) 2330–2340.
- [18] M. Grünbacher, A. Tarjomannejad, P.D.K. Nezhad, C. Praty, K. Ploner, A. Mohammadi, A. Niaezi, B. Klötzer, S. Schwarz, J. Bernardi, Promotion of La (Cu_{0.7}Mn_{0.3})_{0.98} M_{0.02}O_{3-δ} (M = Pd, Pt, Ru and Rh) perovskite catalysts by noble metals for the reduction of NO by CO, *J. Catal.* 379 (2019) 18–32.
- [19] D.D. Beck, J.W. Sommers, C.L. DiMaggio, Impact of sulfur on model palladium-only catalysts under simulated three-way operation, *Appl. Catal. B* 3 (1994) 205–227.
- [20] D. Rainer, M. Koranne, S. Vesecky, D. Goodman, CO+ O₂ and CO+ NO reactions over Pd/Al₂O₃ catalysts, *J. Phys. Chem. B* 101 (1997) 10769–10774.
- [21] J. Summers, J. White, W. Williamson, Durability of palladium only three-way automotive emission control catalysts, *SAE Trans.* (1989) 360–375.
- [22] J.H. Holles, M.A. Switzer, R.J. Davis, Influence of ceria and lanthana promoters on the kinetics of NO and N₂O reduction by CO over alumina-supported palladium and rhodium, *J. Catal.* 190 (2000) 247–260.
- [23] N. Macleod, R. Copley, J.M. Keel, R.M. Lambert, Exploiting the synergy of titania and alumina in lean NO_x reduction: in situ ammonia generation during the Pd/TiO₂/Al₂O₃-catalysed H₂/CO/NO/O₂ reaction, *J. Catal.* 221 (2004) 20–31.
- [24] C. Neyertz, M. Volpe, D. Perez, I. Costilla, M. Sanchez, C. Gigola, NO reduction with CO in the presence and absence of H₂O over Pd/γ-Al₂O₃ and Pd-VO_x/γ-Al₂O₃ catalysts: the formation of HNCO, NH₃ and stable surface species, *Appl. Catal. A* 368 (2009) 146–157.
- [25] J.H. Song, D.C. Park, Y.-W. You, Y.J. Kim, S.M. Kim, I. Heo, D.H. Kim, Kinetic and DRIFTS studies of IrRu/Al₂O₃ catalysts for lean NO_x reduction by CO at low temperature, *Catal. Sci. Technol.* 10 (2020) 8182–8195.
- [26] J. Cortés, E. Valencia, J. Herrera, P. Araya, Mechanism and kinetics parameters of the reduction reaction of NO by CO on Pd/Al₂O₃ catalyst, *J. Phys. Chem. C* 111 (2007) 7063–7070.
- [27] L. Zhang, I.A. Filot, Y.-Q. Su, J.-X. Liu, E.J. Hensen, Transition metal doping of Pd (1 1 1) for the NO+ CO reaction, *J. Catal.* 363 (2018) 154–163.
- [28] E. Fernández, L. Liu, M. Boronat, R. Arenal, P. Concepcion, A. Corma, Low-temperature catalytic NO reduction with CO by subnanometric Pt clusters, *ACS Catal.* 9 (2019) 11530–11541.
- [29] T. Toyao, Y. Jing, K. Kon, T. Hayama, S. Nagaoka, K.-i. Shimizu, Catalytic NO–CO reactions over La-Al₂O₃ supported Pd: promotion effect of La, *Chem. Lett.* 47 (2018) 1036–1039.
- [30] M. Sakai, Y. Nagai, Y. Aoki, N. Takahashi, Investigation into the catalytic reduction of NO_x at copper–ceria interface active sites, *Appl. Catal. A* 510 (2016) 57–63.
- [31] F. Xing, J. Jeon, T. Toyao, K.-i. Shimizu, S. Furukawa, A Cu-Pd single-atom alloy catalyst for highly efficient NO reduction, *Chem. Sci.* 10 (2019) 8292–8298.
- [32] T. Higo, Y. Omori, A. Shigemoto, K. Ueno, S. Ogo, Y. Sekine, Promotive effect of H₂O on low-temperature NO reduction by CO over Pd/La_{0.9}Ba_{0.1}Al_{0.3-δ}, *Catal. Today* 352 (2020) 192–197.
- [33] P.R. Dasari, R. Muncrief, M.P. Harold, Elucidating NH₃ formation during NO_x reduction by CO on Pt-BaO/Al₂O₃ in excess water, *Catal. Today* 184 (2012) 43–53.
- [34] E.C. Adams, M. Skoglundh, M. Folic, E.C. Bendixen, P. Gabrielsson, P.-A. Carlsson, Ammonia formation over supported platinum and palladium catalysts, *Appl. Catal. B* 165 (2015) 10–19.
- [35] C. Asokan, Y. Yang, A. Dang, A.B. Getsoian, P. Christopher, Low-temperature ammonia production during NO reduction by CO is due to atomically dispersed rhodium active sites, *ACS Catal.* 10 (2020) 5217–5222.
- [36] S.A. Hosseini, D. Salari, A. Niaezi, S.A. Oskoui, Physical-chemical property and activity evaluation of LaB_{0.5}Co_{0.5}O₃ (B = Cr, Mn, Cu) and LaMn_xCo_{1-x}O₃ (x = 0.1, 0.25, 0.5) nano perovskites in VOC combustion, *J. Ind. Eng. Chem.* 19 (2013) 1903–1909.

- [37] R. Thalinger, M. Gocyla, M. Heggen, R. Dunin-Borkowski, M. Grünbacher, M. Stöger-Pollach, D. Schmidmair, B. Klötzer, S. Penner, Ni-perovskite interaction and its structural and catalytic consequences in methane steam reforming and methanation reactions, *J. Catal.* 337 (2016) 26–35.
- [38] K. Almusaiter, S.S. Chuang, Dynamic behavior of adsorbed NO and CO under transient conditions on Pd/Al₂O₃, *J. Catal.* 184 (1999) 189–201.
- [39] W. Koehler, E. Wollan, Neutron-diffraction study of the magnetic properties of perovskite-like compounds LaBO₃, *J. Phys. Chem. Solids* 2 (1957) 100–106.
- [40] K. Zorn, S. Giorgio, E. Halwax, C.R. Henry, H. Gronbeck, G. Rupprechter, CO oxidation on technological Pd–Al₂O₃ catalysts: oxidation state and activity, *J. Phys. Chem. C* 115 (2011) 1103–1111.
- [41] J.A. Onrubia-Calvo, B. Pereda-Ayo, A. Bermejo-López, A. Caravaca, P. Vernoux, J. R. González-Velasco, Pd-doped or Pd impregnated 30% La_{0.7}Sr_{0.3}CoO₃/Al₂O₃ catalysts for NO_x storage and reduction, *Appl. Catal. B* 259 (2019), 118052.
- [42] L. Ilieva, G. Pantaleo, J. Sobczak, I. Ivanov, A. Venezia, D. Andreeva, NO reduction by CO in the presence of water over gold supported catalysts on CeO₂-Al₂O₃ mixed support, prepared by mechanochemical activation, *Appl. Catal. B Environ.* 76 (2007) 107–114.
- [43] M. Fernández-García, A. Martínez-Arias, L. Salamanca, J. Coronado, J. Anderson, J. Conesa, J. Soria, Influence of ceria on Pd activity for the CO+O₂ reaction, *J. Catal.* 187 (1999) 474–485.
- [44] W.-J. Shen, M. Okumura, Y. Matsumura, M. Haruta, The influence of the support on the activity and selectivity of Pd in CO hydrogenation, *Appl. Catal. A* 213 (2001) 225–232.
- [45] K. Zhou, H. Chen, Q. Tian, Z. Hao, D. Shen, X. Xu, Pd-containing perovskite-type oxides used for three-way catalysts, *J. Mol. Catal. A Chem.* 189 (2002) 225–232.
- [46] C.-B. Wang, H.-G. Lee, T.-F. Yeh, S.-N. Hsu, K.-S. Chu, Thermal characterization of titania-modified alumina-supported palladium and catalytic properties for methane combustion, *Thermochim. Acta* 401 (2003) 209–216.
- [47] N. Macleod, J. Isaac, R.M. Lambert, Sodium promotion of Pd/γ-Al₂O₃ catalysts operated under simulated “three-way” conditions, *J. Catal.* 198 (2001) 128–135.
- [48] D. Tessier, A. Rakai, F. Bozon-Verduraz, Spectroscopic study of the interaction of carbon monoxide with cationic and metallic palladium in palladium–alumina catalysts, *J. Chem. Soc. Faraday Trans.* 88 (1992) 741–749.
- [49] A. Bensalem, J.-C. Müller, D. Tessier, F. Bozon-Verduraz, Spectroscopic study of CO adsorption on palladium–ceria catalysts, *J. Chem. Soc. Faraday Trans.* 92 (1996) 3233–3237.
- [50] D. Ciuparu, A. Bensalem, L. Pfefferle, Pd–Ce interactions and adsorption properties of palladium: CO and NO TPD studies over Pd–Ce/Al₂O₃ catalysts, *Appl. Catal. B* 26 (2000) 241–255.
- [51] Y. Wang, M. Makke, The influence of CO₂ on NO reduction into N₂ over reduced ceria-based catalyst, *Appl. Catal. B* 221 (2018) 196–205.
- [52] M. Konsolakis, I. Yentekakis, NO reduction by propene or CO over alkali-promoted Pd/YSZ catalysts, *J. Hazard. Mater.* 149 (2007) 619–624.
- [53] D. Lorimer, A. Bell, Reduction of NO by CO over a silica-supported platinum catalyst: infrared and kinetic studies, *J. Catal.* 59 (1979).
- [54] H. Yoshida, K. Koizumi, M. Boero, M. Ehara, S. Misumi, A. Matsumoto, Y. Kuzuhara, T. Sato, J. Ohyama, M. Machida, High turnover frequency CO–NO reactions over Rh overlayer catalysts: a comparative study using Rh nanoparticles, *J. Phys. Chem. C* 123 (2019) 6080–6089.
- [55] C.-J. Yoo, A.B. Getsoian, A. Bhan, NH₃ formation pathways from NO reduction by CO in the presence of water over Rh/Al₂O₃, *Appl. Catal. B* 286 (2021), 119893.
- [56] M. Shelef, H.S. Gandhi, Ammonia formation in catalytic reduction of nitric oxide by molecular hydrogen. I. Base metal oxide catalysts, *Ind. Eng. Chem. Prod. Res. Dev.* 11 (1972) 2–11.